Article type: Full Paper

Dopant-Free Small Molecule Hole-transporting Material for Inverted Perovskite Solar Cells with Efficiency Exceeding 21%

Yang Wang, Wei Chen, Lei Wang, Bao Tu, Tian Chen, Bin Liu, Kun Yang, Chang Woo Koh, Xianhe Zhang, Huiliang Sun, Guocong Chen, Xiyuan Feng, Han Young Woo, Aleksandra B. Djurišić, Zhubing He* and Xugang Guo**

Dr. Y. Wang, W. Chen, Dr. L. Wang, B. Tu, T. Chen, B. Liu, Dr. K. Yang, X. Zhang, Dr. H. Sun, G. Chen, X. Feng, Prof. Z. He, Prof. X. Guo
Department of Materials Science and Engineering, Southern University of Science and Technology (SUSTech), No. 1088, Xueyuan Road, Shenzhen, Guangdong 518055, China.
E-mail: hezb@sustech.edu.cn; guoxg@sustech.edu.cn
W. Chen, Prof. A. B. Djurišić
Department of Physics, The University of Hong Kong, Pokfulam, Hong Kong SAR.
E-mail: dalek@hku.hk
C. W. Koh, Prof. H. Y. Woo
Department of Chemistry, Korea University, Seoul 02841, South Korea.
Dr. Y. Wang
Key Laboratory of Functional Polymer Materials and State Key Laboratory of Medicinal Chemical Biology, The Co-Innovation Center of Chemistry and Chemical Engineering of Tianjin, Institute of Polymer Chemistry, College of Chemistry, Nankai University, Tianjin 300071, China.

1

Abstract

Hole-transporting materials (HTMs) play a critical role in realizing efficient and stable perovskite solar cells (PVSCs). Considering their capability of enabling PVSCs with good device reproducibility and long-term stability, high-performance dopant-free small molecule HTMs (SM-HTMs) are greatly desired. However, such dopant-free SM-HTMs are highly elusive, limiting the current record efficiencies of inverted PVSCs to around 19%. Here, we devised two novel donor-acceptor (D-A) type SM-HTMs (MPA-BTI and MPA-BTTI), which synergistically integrate several design principles for high-performance HTMs, and exhibit comparable optoelectronic properties but distinct molecular configuration and film properties. Consequently, the dopant-free MPA-BTTI based inverted PVSCs achieved a remarkably high efficiency of 21.17% with negligible hysteresis and superior thermal stability and long-term stability under illumination, which breaks the long-time standing bottleneck in the development of dopant-free SM-HTMs for highly efficient inverted PVSCs. Such breakthrough is attributed to the well-aligned energy levels, appropriate hole mobility, and most importantly, the excellent film morphology of the MPA-BTTI. The results underscore the effectiveness of our design tactics, providing a new avenue for developing high-performance dopant-free SM-HTMs in PVSCs.

Metal halide perovskite solar cells (PVSCs) have attracted a great deal of attention from both scientific and industrial communities in the past few years due to their intriguing photophysical properties, high power conversion efficiencies (PCEs), and great potential for low-cost solution processing.[1,2] There are three typical device architectures of PVSCs: mesoporous structure, planar n-i-p (or conventional) structure and p-i-n (or inverted) structure.[1] While the record efficiencies of inverted PVSCs are generally lower compared to those of conventional ones (both planar and mesoscopic), inverted PVSCs are more compatible with low-temperature processing and generally exhibit suppressed hysteresis effect.[3-5] In addition, the inverted architecture is also suitable for improving the efficiency of silicon/perovskite tandem cells.[6] Therefore, there is considerable interest in improving the device performance of inverted PVSCs.

In inverted PVSCs, in addition to compositional modulation of the perovskite absorber, interfacial engineering plays a decisive role in achieving high efficiency and long-term stability.[7-9] The interface properties between perovskite absorber and hole-transporting material (HTM, or p-layer in p-i-n structure) are critically dependent on the HTM. There are three classes of HTMs utilized in PVSCs, namely inorganic HTMs, polymeric HTMs, and organic small molecule HTMs (SM-HTMs).[10-13] Inorganic HTMs[5,14-16] usually show good device stability, but the achievable PCE is limited by their relatively low intrinsic conductivity and surface defects.[17] Polymeric HTMs[18,19] result in good morphological properties but inferior reproducibility and stability, in particular when dopants are needed for high efficiency devices.[20] A possible solution to address the issues associated with the current HTMs to achieve highly efficient PVSCs with facile processability, good performance reproducibility, and long-term stability is the use of dopant-free SM-HTMs.[21-23] However, the highest reported efficiencies to date are still around 19% (Figure 1a and Table S1).[24] Therefore, exploring new SM-HTMs to further improve the device performance of PVSCs is urgent. Ideal dopant-free SM-HTMs should have good solubility in common solvents, high thermal stability (i.e. high decomposition temperature (T_d) and glass transition temperature (T_g)),[25] low absorption in visible region,[27] suitable energy level alignment with perovskite absorber,[27] and high hole mobility and conductivity.[23,28] In addition to these general criteria for ensuring good film quality and minimizing optical and electrical losses, several molecular design principles are also identified for achieving highly efficient dopant-free SM-HTMs. Firstly, donor-acceptor (D-A) molecular backbone is conceived a desirable structural feature due to its intramolecular charge transfer (ICT) character and high dipole moment, which could induce self-doping and built-in potential to boost charge extraction.[29,30] Secondly,

bis(4-methoxyphenyl)amine has been identified as the preferential hole-transporting moiety to improve charge mobility at molecular level due to its easy oxidizability and its ability to effectively transport positive charge. Also, the pseudo-3D conjugated architecture of triphenylamine building block may endow molecules with isotropic charge transport property.[31,32] Thirdly, reinforced intermolecular interactions and π-π stacking are expected to result in to achieve high conductivity, which could be achieved by employing planar building blocks widely used in organic field-effect transistors or thermoelectrics, such as thiophene-based derivatives.[33] Moreover, sulfur (S) atoms can passivate defects in perovskite by coordinating Pb^{2+} vacancies.[34] Finally, Lewis base groups (e.g. carbonyl and cyano substituent) capable of passivating defects[35,36] are hence desired to be incorporated to enhance the passivation of perovskite layer.

Based on these considerations, in this work we design and synthesize two imide-functionalized thiophene based HTMs, 2,8-bis(4-(bis(4-methoxyphenyl)amino)phenyl)-5-octyl-4H-dithieno[3,2-c:2',3'-e]azepine-4,6(5H)-dione and 2,8-bis(4-(bis(4-methoxyphenyl) amino)phenyl)-5-dodecyl-4H-thieno[2',3':4,5]thieno[3,2-c]thieno[2',3':4,5]thieno[2,3-e] azepine-4,6(5H)-dione (Figure 1b, designated as MPA-BTI and MPA-BTTI, respectively). These molecules show comparable photophysical and electrochemical properties but remarkably distinct molecular configuration, packing characteristics, and the resultant film morphology. When utilized as the dopant-free SM-HTMs in inverted PVSCs, the MPA-BTTI based device achieves an unprecedented performance showing a champion PCE of 21.17% with a V_{oc} of 1.12, a J_{sc} of 23.23 mA cm^{-2}, and a FF of 0.81, which outperforms the MPA-BTI based device with a PCE of 17.20%. The efficiency (21.17%) is approaching the highest value (21.6%) achieved in inverted single-junction PVSCs reported to date.[37] Furthermore, the MPA-BTTI based device exhibits negligible hysteresis (21.17% and 21.01% for reverse and forward scans, respectively) and excellent long-term thermal stability and stability under illumination. The devices retain 90% of the original PCE after 500 h constant illumination and 94% of initial PCE after thermal stress at 80 °C for 800 h in inert environment. The exceptional performance of the device with the MPA-BTTI SM-HTM can be attributed to its well-matched energy level, appropriate hole mobility, and most importantly, excellent film morphological property (i.e. smooth surface, high thermal stability, increased hydrophobicity, and improved passivation effect) which enables the growth of high-quality perovskite active layer and superior interfacial contact. These results demonstrate the remarkable potential of our proposed molecular design principles for highly efficient dopant-free HTMs.

Based on the design principles described above for an ideal SM-HTM, we adopted 4-methoxy-*N*-(4-methoxyphenyl)-*N*-phenylaniline as the donor fragment and imide-functionalized thiophene derivative as the acceptor moiety to construct D-A type molecules. The phenylamine groups enable efficient hole transport, while the imide-functionalized cores can simultaneously ensure good intermolecular π-π stacking due to their planar molecular structures, result in passivation effect *via* carbonyl groups, and lead to good solubility via *N*-alkylation. Moreover, the backbone of the acceptor moiety is varied from 2,2'-bithiophene (MPA-BTI) to 2,2'-bithieno[3,2-b]thiophene (MPA-BTTI) in order to tune molecular configurations as well as the resultant optoelectronic and film morphological properties.[22b]

The synthetic route to these SM-HTMs is straightforward (Figure S1). Starting from the previously reported thiophene-based anhydrides 1 and 5,[38,39] the imidization was carried out via an improved method using 4-dimethylaminopyridine for ring-opening reaction followed by acetic anhydride-assisted ring-closure reaction. Note that *n*-octyl chain and *n*-dodecyl chain are selected for MPA-BTI and MPA-BTTI, respectively, to obtain adequate solubility for synthesizing the subsequent intermediates and final SM-HTMs. Then compounds 3 and 7 were obtained using different brominating reagents, i.e. bromine (Br_2) and *N*-bromosuccinimide (NBS), respectively, due to the distinct reactivity of 2 and 6. Finally, Suzuki coupling of 3 and 7 with boric ester 4 produced the target materials MPA-BTI and MPA-BTTI, respectively, in moderate overall yields (~30%). The chemical structures of MPA-BTI and MPA-BTTI were well characterized by ^{1}H NMR, ^{13}C NMR, high resolution mass spectrometry (HRMS), and elemental analysis (EA). The two materials exhibit good solubility in common organic solvents, such as dichloromethane (CH_2Cl_2), tetrahydrofuran and toluene *etc*., but marginal solubility in highly polar solvents like dimethyl sulfoxide (DMSO), hence ensuring their good solution processability and tolerance to perovskite precursor solutions.

Density functional theory (DFT) and time-dependent DFT (TD-DFT) were utilized to provide insights into molecular geometries, frontier molecular orbital (FMO) energy levels, dipole moments as well as electronic transition energies of MPA-BTI and MPA-BTTI at the B3LYP/6-31(d) level. As shown in Figure 2, these imide-functionalized thiophene based electron-deficient cores feature highly planar backbone but enable distinct backbone configurations for the whole molecules, i.e. V-shaped and linear structures for MPA-BTI and MPA-BTTI, respectively, which in turn can significantly affect film morphologies which will be described in detail later. The highest occupied molecular orbitals (HOMOs) of MPA-BTI and MPA-BTTI are mainly localized on triphenylamine moieties and partly on the acceptor

cores, while the lowest unoccupied molecular orbitals (LUMOs) are concentrated on the acceptor cores. As anticipated, the introduction of an additional thiophene in MPA-BTTI results in the lowered LUMO energy level, elevated HOMO energy level, and hence narrower bandgap due to the elongation of π-conjugation. Additionally, the calculated dipole moments of MPA-BTI and MPA-BTTI are 6.74 and 4.78 D, respectively, much larger than those of benchmark Spiro-OMeTAD (0.28 D) and PTAA (0.27 D),[29] owing to their intrinsic D-A structures. Such structure leads to broad absorption, which can be confirmed by the TD-DFT calculation (Figure S2 and Table S2). The simulated absorption spectra show an ICT absorption in the long wavelength region (550-650 nm) which features dominant transition from HOMOs on donor units to LUMOs on acceptor units, while the absorption in the short wavelength region (<400 nm) can be attributed to π-π^* transitions. Furthermore, the images of electrostatic potential surface (EPS) were illustrated in Figure 2c. Dominant positive charges are delocalized on the triphenylamine groups, while the carbonyl groups feature the most significant negative charges, which can act as Lewis base anchors to passivate perovskite defects.[35] Finally, hole reorganization energies (λ_hs) were also calculated to provide insights into the charge transport capacity (Table S3). Compared to that (0.49 eV) of Spiro-OMeTAD reported in literature,[40] very low λ_h values of 0.18 and 0.15 eV are obtained for MPA-BTI and MPA-BTTI, respectively, indicative of the improved hole mobility of our materials.

The optical properties of MPA-BTI and MPA-BTTI in both solution and solid state were characterized. The UV-vis absorption spectra are shown in Figure 3a, while the relevant parameters are presented in Table 1. Two distinct absorption peaks, assigned to the ICT absorption and π-π^* transition, respectively, were observed for both MPA-BTI (335 and 487 nm) and MPA-BTTI (343 and 532 nm), in good agreement with the DFT calculations.. In solid state, the absorption profile of MPA-BTI becomes broadened and red-shifted likely due to the formation of *J*-aggregates as commonly observed in many π-conjugated molecules. In contrast, a hypsochromic shift (~ 10 nm) from 532 nm to 522 nm was found for MPA-BTTI, likely attributed to *H*-aggregation in solid state. This is reasonable given that MPA-BTTI features a more extended π-system with symmetrical structure and improved planarity, which is beneficial for face-to-face molecular packing. This phenomenon is ubiquitous in metal phthalocyanine based molecules, which exhibits specific *H*-aggregation in thin films due to their pronouncedly large and planar structures.[41] Such different packing characteristics between MPA-BTI and MPA-BTTI can significantly affect the film morphologies. It should be noted that although such D-A molecules can lead to the absorption in the visible region, the impact of this on solar cell performance can be attenuated by using a thin layer of the SM-

HTMs, which can be constrained to below ~10 nm. Consequently, the transmittance still remains above 65% in the range of 400-650 nm. As shown in Figure S3, this is only ~10% less than that of the bare ITO glass substrate, ensuring that the majority of the photons can reach the perovskite active layer.

Electrochemical properties of these SM-HTMs were measured next by cyclic voltammetry (CV), and the cyclic voltammograms are shown in Figure 3b, while the relevant data are included in Table 1. Evident oxidative and reductive processes could be observed for both MPA-BTI and MPA-BTTI with similar profiles. With ferrocene/ferrocenium redox as the reference, the HOMO levels of MPA-BTI and MPA-BTTI are determined to be -5.28 and -5.24 eV, respectively, and the LUMO levels are calculated to be -3.15 and -3.32 eV, respectively.[13,41] The up-shifted HOMO level, the down-shifted LUMO level, and the resultant narrower bandgap from MPA-BTI to MPA-BTTI are in good agreement with the DFT calculation results. To further confirm the energy levels in solid state, ultraviolet photoelectron spectroscopy (UPS) was used to characterize the HOMO levels of MPA-BTI and MPA-BTTI films. The cut-off ($E_{cut-off}$) and onset (E_{onset}) energy regions in the UPS spectra are shown in Figure S4. According to the equation: $\Phi = 21.2 - (E_{cut-off} - E_{onset})$,[30] the HOMO levels of MPA-BTI and MPA-BTTI are calculated to be -5.36 and -5.32 eV, respectively. By subtracting the optical bandgap (E_g^{opt}) in solid state from HOMO level, the LUMO levels are evaluated to be -3.24 and -3.40 eV, respectively, which are close to the results determined from CV measurements. More importantly, the energy levels obtained from solid state suggest that the HOMO levels of such SM-HTMs match well with the perovskite layer (~5.4 eV) to enhance hole extraction, and simultaneously the LUMO levels are shallow enough to block electron leakage.

To further evaluate the properties of MPA-BTI and MPA-BTTI, the thermal stability of films was probed. As shown in Table 1 and Figure S5, the thermogravimetric analysis (TGA) reveals nearly the same decomposition temperatures (T_ds) of MPA-BTI (432 $^{\circ}$C) and MPA-BTTI (431 $^{\circ}$C). However, the differential scanning calorimetry (DSC) shows clearly distinct thermal properties of two HTMs (see Figure 3c). For MPA-BTI, a low glass transition temperatures (T_g) of 86 $^{\circ}$C is detected during the second heating scan, followed by an exothermic peak at ~200 $^{\circ}$C as well as a melting temperature approaching 250 $^{\circ}$C. While for MPA-BTTI, only a T_g of 256 $^{\circ}$C is observed, higher than that of MPA-BTI and even much higher than that of Spiro-OMeTAD (121 $^{\circ}$C).[24] The good thermal stability and high T_g of MPA-BTTI is essential for device fabrication and shelf-life stability of PVSCs, in particular in inverted architecture where perovskite is deposited on top of the HTM and then annealed at

elevated temperature. In addition, surface wettability of these novel HTMs was investigated because a relatively hydrophobic surface can facilitate the growth of high-quality perovskite polycrystalline films as well as preclude water permeation.[42] The contact angle measurements show that MPA-BTI exhibits a modest contact angle of 59.1 ℃ to water droplet, which is higher than both PEDOT:PSS (16.9 ℃) and Spiro-OMeTAD (38.7 ℃)[23] (see Figure S6). More encouragingly, MPA-BTTI possesses a much larger angle of 83.8 ℃, and therefore a greatly increased hydrophobicity compared to MPA-BTI.

Atomic force microscopy (AFM) was then performed to examine the surface morphology of both HTMs. As shown in Figure S7, MPA-BTTI exhibits a smoother and more homogeneous surface with a root-mean-square roughness (R_q) of 0.44 nm compared to MPA-BTI with a R_q of 0.96 nm. Moreover, the molecular ordering of both HTMs in bulk thin films was investigated by two-dimensional grazing-incidence wide-angle X-ray scattering (2D-GIWAXS) (Figure S8). Both SM-HTMs show a weak π-π stacking peak either along the out-of-plane direction or in-plane direction, indicating nearly amorphous nature of the MPA-BTI and MPA-BTTI pristine films. Nevertheless, it was found that superior film uniformity and morphological stability could be even more important than hole mobility in determining device performance of PVSCs.[43,44] Based on space charge-limited current (SCLC) method, the hole mobility of neat MPA-BTI film is determined to be 3.99×10^{-5} cm^2 V^{-1} s^{-1} which is comparable to that (2.13×10^{-5} cm^2 V^{-1} s^{-1}) of the widely used Spiro-OMeTAD.[23] Encouragingly, MPA-BTTI shows a much higher hole mobility of 2.02×10^{-4} cm^2 V^{-1} s^{-1} despite of its amorphous character (Table 1 and Figure S9), which is in good agreement with the trend of the calculated λ_h values. Similarly, the measured conductivity of undoped MPA-BTTI film is higher than that of MPA-BTI (1.35×10^{-5} *vs* 6.90×10^{-6} S cm^{-1}) (Table 1 and Figure S10), which is comparable to that of undoped Spiro-OMeTAD (~10^{-5} S cm^{-1}).[45] Thus, pristine MPA-BTTI possesses promising hole-transporting capacity, which favorably allows it to function as an effective HTM in PVSCs without extra doping process.

To evaluate the device performance of these two small molecules as dopant-free HTMs in inverted perovskite solar cells, the widely-used device configuration of ITO/SM-HTMs/perovskite/C$_{60}$/bathocuproine(BCP)/Ag was adopted (Figure 4a). The active perovskite layer with mixed Cs$^+$, HC(NH)$_2$$^+$ and CH$_3$NH$_3$$^+$ cations (CsFAMA for simplicity) was prepared using the one-step antisolvent method,[14,46] while the SM-HTMs were optimized by varying concentrations in toluene and annealing temperatures. It was found that the concentration of 3.5 mg/mL in toluene (for MPA-BTI and MPA-BTTI), and 80 ℃ and 110 ℃

thermal annealing for MPA-BTI and MPA-BTTI, respectively, yielded the optimal conditions to achieve the best device performance (Figure S11).

Figure 4c displays the current density-voltage (J-V) curves for the optimal devices under the standard AM 1.5G illumination, and the corresponding data are summarized in Table 2. The MPA-BTI based device achieved an encouraging PCE of 17.20% with a J_{sc} of 21.58 mA cm^{-2}, a V_{oc} of 1.09, and FF of 73.14%, and the device also showed a small hysteresis with a PCE of 16.72% for the forward scan. The MPA-BTTI based device yielded an astonishingly high PCE of 21.17% with a J_{sc} of 23.23 mA cm^{-2}, a V_{oc} of 1.12, and a FF of 81.35%. More importantly, there is a negligible hysteresis during the forward scan, with a PCE of 21.02% with a J_{sc} of 23.26 mA cm^{-2}, a V_{oc} of 1.12, and a FF of 80.60%. The corresponding external quantum efficiency (EQE) spectra are shown in Figure 4e, which correspond to integrated current densities of 20.75 and 22.39 mA cm^{-2} for the MPA-BTI and MPA-BTTI based PVSCs, respectively, in good agreement with the results from J-V curves. To further confirm the efficiencies obtained from the J-V curves, the current densities as a function of time at the maximum power point, (i.e. 0.88 V and 0.95 V for MPA-BTI and MPA-BTTI, respectively) were evaluated, and Figure 4d shows the stabilized PCE of 16.98% and 21.02 % after 500 s duration for the MPA-BTI and MPA-BTTI based devices, respectively, indicating a high reliability of our J-V curves. Moreover, good reproducibility is achieved for MPA-BTTI based devices as shown in Figure 4f, where the efficiency histogram shows that >70% of the devices (~40 devices) have a PCE higher than 20.7%. To highlight the unprecedented efficiency achieved by MPA-BTTI, the control devices with widely-used HTMs such as PEDOT:PSS, NiO$_x$ and PTAA were also fabricated (Figure S12 and Table 4). For optimal fabrication conditions, these devices showed the maximum PCEs of 17.11%, 19.49% and 19.85%, respectively, under the optimal fabrication conditions, which are significantly lower compared to that of the MPA-BTTI based device.

As discussed above, MPA-BTI and MPA-BTTI possess similar photophysical and electrochemical properties but greatly different molecular configuration which will affect not only the intrinsic hole-transporting capacity but also the material packing motif and the resultant film morphology. Since the hole mobility and conductivity of MPA-BTTI is indeed not very high compared to other SM-HTMs reported in the literature,[23,41,45] hence the ultrahigh efficiency achieved by MPA-BTTI is most likely related to the film morphology, which can dominate the growth of perovskite active layer and largely affect the interfacial contact. To probe the effects of SM-HTMs on perovskite formation, scanning electron microscopy (SEM) was first performed and the images are shown in Figure S13. Apparently,

the average size (~400 nm) of perovskite grains on MPA-BTTI is larger than that (~320 nm) on MPA-BTI. Furthermore, the higher intensity of X-ray diffraction (XRD) peaks of perovskite films on MPA-BTTI indicates its greater film crystallinity (Figure S14). Based on the cross-section SEM images (Figure 4b), we can clearly observe smooth multilayer structure and compact perovskite films for the MPA-BTTI based device with very large crystalline grains. The increased grain size is likely contributed to two factors, namely the increased hydrophobicity and the improved thermal stability of MPA-BTTI. The smooth and hydrophobic surface of MPA-BTTI facilitates the growth of large size perovskite grains by suppressing heterogeneous nucleation.[42] Increased thermal stability of MPA-BTTI compared to MPA-BTI contributes to improved quality of perovskite films due to the fact that annealing step in the preparation of CsFAMA perovskite (at 100ºC) will induce phase transition in the underlying MPA-BTI film with a low T_g of 86ºC, which could adversely affect the perovskite growth. We can already observe that MPA-BTI annealed at 80ºC exhibits higher roughness compared to MPA-BTTI annealed at 110ºC (Figure S7). Consequently, the excellent morphological and thermal properties of MPA-BTTI result in the formation of high-quality perovskite polycrystalline film with low degree of defects, which enhances J_{sc} and FF in PVSCs due to the better light-harvesting capability and prolonged carrier diffusion length.

Fourier transform infrared (FTIR) spectroscopy was conducted to further probe the HTM/perovskite interfaces. As reported in the literature, functional groups with lone electron pairs such as carbonyl and cyano groups can form coordination sites with Pb defects in perovskite film.[35,36] Hence, FTIR spectra of pure MPA-BTI and MPA-BTTI, and the mixed films of MPA-BTI/PbI$_2$ and MPA-BTTI/PbI$_2$ were characterized. As shown in Figure S15, the stretching vibration of carbonyl groups in MPA-BTI and MPA-BTTI is located at 1652 and 1640 cm^{-1}, respectively, and additional peaks at 1701 and 1699 cm^{-1} appear after blending with PbI$_2$, which suggests the existence of interaction between SM-HTMs and Pb ions in the perovskite films. In addition, normalized steady-state photoluminescence (PL) spectra at room temperature can further confirm such interactions. As shown in Figure S16, the emission peak of perovskite deposited on the SM-HTM is slightly blue-shifted (~ 5 nm), which is consistent with the findings in previous reports.[42,47] The good interfacial contact may passivate defects at HTM/perovskite interface and consequently reduce recombination loss and enhance device efficiency.

To investigate the non-radiative recombination losses in PVSCs, the steady-state PL spectra were measured, as shown in Figure S17. The PL intensity was quenched sharply for the MPA-BTI/perovskite film and more significantly for the MPA-BTTI/perovskite film,

which indicates more efficient hole transfer at the interface between MPA-BTTI and perovskite layer. Then, the time-resolved photoluminescence (TRPL) measurements were carried out as illustrated in Figure S18 with the data of carrier lifetime summarized in Table S5. All of PL decay curves exhibit bi-exponential lifetimes with an initial fast decay (τ_1) and second slow decay (τ_2). As elaborated in the literature,[37,48] such decay may originate from either the extraction of charges (~ (sub)nanosecond timescales) or non-radiative recombination losses (~ hundreds of nanosecond timescales). Following this principle, we can attribute the fast decay (τ_1) to the charge extraction to the HTMs and/or partly to the interface recombination, and the second slow decay (τ_2) mainly to interface recombination losses. Compared to a perovskite film on ITO substrate (τ_1 = 12.4 ns, τ_2 = 822.8 ns), the perovskite on MPA-BTTI shows a sharply shortened τ_1 of 3.3 ns and a moderately decreased τ_2 of 484.2 ns. However, the perovskite on MPA-BTI exhibits a prolonged τ_1 of 46.5 ns and a drastically reduced τ_2 of 171.8 ns, which suggests that hole extraction is more efficient from perovskite to MPA-BTTI than from perovskite to MPA-BTI. At the same time, non-radiative recombination losses are significantly lower at the MPA-BTTI/perovskite interface compared to the MPA-BTI/perovskite interface, although the average lifetime (τ_{avg}) of MPA-BTI seems to be shorter than MPA-BTTI. Therefore, the enhanced hole extraction and reduced non-radiative recombination of MPA-BTTI based PVSC contributes to the higher V_{oc} and FF compared to MPA-BTI one.

Overall, our work indicates that when designing efficient dopant-free HTMs for high-performance inverted PVSCs, in addition to transmittance, energy level alignment and hole mobility, the molecular structure and the resulting film morphology play a critical role in determining perovskite growth and interfacial interactions. The smooth and non-wetting film of HTMs is more likely to facilitate the formation of high quality perovskite films. In addition, high thermal stability is highly beneficial for preserving the quality of the HTM/perovskite interface and the growth of high quality perovskite film. In the case of MPA-BTI, we can already observe increased surface roughness after annealing at 80 ºC, which is lower than its T_g (86 ºC) and lower than the annealing temperature of CsFAMA perovskite film (100ºC). Furthermore, the incorporation of passivation groups into HTMs enables the interfacial optimization and inhibition of carrier recombination, leading to improved device efficiency.

In addition to power conversion efficiency, long-term device stability is essential for commercialization of PVSCs.[1] Due to the low efficiency of MPA-BTI based device, we only investigated the device stability of MPA-BTTI based solar cell and compared it with other widely-used HTMs (i.e. PEDOT:PSS, PTAA, and NiO$_x$). We firstly evaluated the long-term

stability in the dark in a dry box environment (~20% RH). As shown in Figure S19, the PEDOT:PSS based device shows the poorest stability with only 50% of initial PCE retained after 15 days. The inferior stability of devices with PEDOT:PSS can be attributed to its hygroscopic character. The PTAA and NiO_x based devices exhibit similar stability with 80% and 85% of their original PCEs retained after 40 days storage, respectively. Encouragingly, the best stability is achieved in the MPA-BTTI based device which maintains 90% of initial PCE after 60 days. The stability of encapsulated solar cell device under continuous light irradiation in ambient environment (~25 $^{\circ}$C, 30-40% humidity) was then investigated. PEDOT:PSS based device is not included in the light stability tests due to their clearly inferior stability in the dark storage tests. We can observe that the MPA-BTTI based device possesses much higher light stability than the PTAA based one (Figure S20). We further measured the operational stability of the MPA-BTTI based device by maximum power point (MPP), which are shown in Figure 5a, demonstrating that 90% of initial PCE could be maintained after ~500 h continuous illumination. Furthermore, thermal stability characterization shows that the MPA-BTTI based device can retain 94% of its initial PCE after thermal stress at 80 °C for 800 h in glove box, which is comparable with the thermal stability of NiO_x based device and much better than PTAA based device (Figure 5b and Figure S21). The good long-term stability of the MPA-BTTI based device could be attributed to the excellent morphological properties of the underlying MPA-BTTI film, which facilitate favorable interfacial interactions between HTM and perovskite, enable compact perovskite growth, reduce grain boundaries and surface defects, and inhibit various processes leading to the performance degradation, such as water penetration, perovskite decomposition, ion migration, and other undesirable changes.[49,50]

In summary, two novel D-A type SM-HTMs with phenylamine groups as the D units and imide-functionalized thiophene derivatives as the A units were rationally developed based on the identified molecular design principles. Both SM-HTMs show similar photophysical and electrochemical properties but greatly different molecular configuration and film morphological properties. While there is a complex interplay between HTM properties and device performance, we found that the film morphology played more important part in determining the device performance compared to transmittance, energy level alignment and hole mobility. This is likely due to significant effects of underlying film properties on the crystallization of the perovskite film which is deposited on top, as well as the interface quality and consequently interfacial recombination losses. Hence, due to good energy level alignment, appropriate hole-transporting ability, and most importantly, the excellent film morphology (i.e.

high thermal stability, smooth surface, increased hydrophobicity, and improved passivation effect), MPA-BTTI based PVSC exhibits an excellent PCE of 21.17% with a V_{oc} of 1.12, a J_{sc} of 23.23 mA cm^{-2}, and a FF of ~81% as well as a negligible hysteresis, marking the record PCE value for PVSCs with dopant-free SM-HTMs reported to date. More importantly, good long-term stability was realized in the MPA-BTTI based device which retains 90% of its initial PCE after 500 h constant illumination and simultaneously maintains 94% of its initial PCE after 800 h thermal stress at 80 °C. The study not only breaks the long-time standing bottleneck in the development of dopant-free SM-HTMs but also paves the way to explore other dopant-free SM-HTMs for highly efficient inverted PVSCs.

Supporting Information
Supporting Information is available from the Wiley Online Library or from the author.

ORCID

Yang Wang: 0000-0002-3669-0192

Han Young Woo: 0000-0001-5650-7482

Aleksandra B. Djurišić: 0000-0002-5183-1467

Xugang Guo: 0000-0001-6193-637X

Zhubing He: 0000-0002-2775-0894

Conflict of Interest
The authors declare no conflict of interest.

[1] Y. G. Rong, Y. Hu, A. Mei, H. Tan, M. Saidaminov, S. I. Seok, M. D. McGehee, E. H. Sargent, H. Han, *Science* **2018**, *361*, eaat8235.

[2] H. J. Snaith, *Nat. Mater.* **2018**, *17*, 372.

[3] J. Y. Jeng, Y. F. Chiang, M. H. Lee, S. R. Peng, T. F. Guo, P. Chen, T. C. Wen, *Adv. Mater.* **2013**, *25*, 3727.

[4] F. Di Giacomo, A. Fakharuddin, R. Jose, T. M. Brown, *Energy Environ. Sci.* **2016**, *9*, 3007.

[5] J. B. You, L. Meng, T. B. Song, T. F. Guo, Y. Yang, W. H. Chang, Z. R. Hong, H. J. Chen, H. P. Zhou, Q. Chen, Y. S. Liu, N. De Marco, Y. Yang, *Nat. Nanotechnol.* **2016**, *11*, 75.

[6] B. Chen, X. P. Zheng, Y. Bai, N. P. Padture, J. S. Huang, *Adv. Energy Mater.* **2017**, *7*, 1602400.

[7] Y. Bai, X. Y. Meng, S. H. Yang, *Adv. Energy Mater.* **2018**, *8*, 1701883.

[8] B. Roose, Q. Wang, A. Abate, *Adv. Energy Mater.* **2019**, *9*, 1803140.

[9] C. C. Chueh, C. Z. Li, A. K. Y. Jen, *Energy Environ. Sci.* **2015**, *8*, 1160.

[10] W. B. Yan, S. Y. Ye, Y. L. Li, W. H. Sun, H. X. Rao, Z. W. Liu, Z. Q. Bian, C. Huang, *Adv. Energy Mater.* **2016**, *6*, 1600474.

[11] A. Krishna, A. C. Grimsdale, *J. Mater. Chem. A* **2017**, *5*, 16446.

[12] M. A. Haque, A. D. Sheikh, X. Guan, T. Wu, *Adv. Energy Mater.* **2017**, *7*, 1602803.

[13] a) Y. Wang, Z. L. Zhu, C. C. Cheuh, A. K. Y. Jen, Y. Chi, *Adv. Energy Mater.* **2017**, *7*, 1700823; b) H. D. Pham, X. Li, W. Li, S. Manzhos, A. K. K. Kyaw, P. Sonar, *Energy. Environ, Sci.* **2019**, *12*, 1177.

[14] W. Chen, Y. Zhou, L. Wang, Y. Wu, B. Tu, B. Yu, F. Liu, H.-W. Tam, G. Wang, A. B. Djurišić, L. Huang, Z. He, *Adv. Mater.* **2018**, *30*, 1800515.

[15] S. Y. Ye, H. X. Rao, W. B. Yan, Y. L. Li, W. H. Sun, H. T. Peng, Z. W. Liu, Z. Q. Bian, Y. F. Li, C. H. Huang, *Adv. Mater.* **2016**, *28*, 9648.

[16] W. Chen, Y. Z. Wu, Y. F. Yue, J. Liu, W. J. Zhang, X. D. Yang, H. Chen, E. B. Bi, I. Ashraful, M. Grätzel, L. Y. Han, *Science* **2015**, *350*, 944.

[17] W. Chen, Y. H. Wu, J. Fan, A. B. Djurišić, F. Z. Liu, H. W. Tam, A. Ng, C. Surya, W. K. Chan, D. Wang, Z. B. He, *Adv. Energy Mater.* **2018**, *8*, 1703519.

[18] W. Y. Nie, H. H. Tsai, R. Asadpour, J. C. Blancon, A. J. Neukirch, G. Gupta, J. J. Crochet, M. Chhowalla, S. Tretiak, M. A. Alam, H. L. Wang, A. D. Mohite, *Science* **2015**, *347*, 522.

[19] X. P. Zheng, B. Chen, J. Dai, Y. J. Fang, Y. Bai, Y. Z. Lin, H. T. Wei, X. C. Zeng, J. S. Huang, *Nat. Energy* **2017**, *2*, 17102.

[20] D. Y. Luo, W. Q. Yang, Z. P. Wang, A. Sadhanala, Q. Hu, R. Su, R. Shivanna, G. F. Trindade, J. F. Watts, Z. J. Xu, T. H. Liu, K. Chen, F. J. Ye, P. Wu, L. C. Zhao, J. Wu, Y. G. Tu, Y. F. Zhang, X. Y. Yang, W. Zhang, R. H. Friend, Q. H. Gong, H. J. Snaith, R. Zhu, *Science* **2018**, *360*, 1442.

[21] C. Rodríguez-Seco, L. Cabau, A. Vidal-Ferran, E. Palomares, *Acc. Chem. Res*. **2018**, *51*, 869.

[22] a) R. Shang, Z. M. Zhou, H. Nishioka, H. Halim, S. Furukawa, I. Takei, N. Ninomiya, E. Nakamura, *J. Am. Chem. Soc*. **2018**, *140,* 5018; b) H. D. Pham, L. Gil-Escrig, K. Feron, S. Manzhos, S. Albrecht, H. J. Bolink, P. Sonar, *J. Mater. Chem. A*, **2019**, *7*, 12507.

[23] a) C. Y. Huang, W. F. Fu, C. Z. Li, Z. Q. Zhang, W. M. Qiu, M. M. Shi, P. Heremans, A. K. Y. Jen, H. Z. Chen, *J. Am. Chem. Soc*. **2016**, 138, 2528; b) H. D. Pham, K. Hayasake, J. Kim, T. T. Do, H. Matsui, S. Manzhos, K. Feron, S. Tokito, T. Watson, W. C. Tsoi, N. Motta, J. R. Durrant, S. M. Jain, P. Sonar, *J. Mater. Chem. C* **2018**, *6*, 3699.

[24] L. Y. Yang, F. L. Cai, Y. Yan, J. H. Li, D. Liu, A. J. Pearson, T. Wang, *Adv. Funct. Mater*. **2017**, *27*, 1702613.

[25] K. Rakstys, M. Saliba, P. Gao, P. Gratia, E. Kamarauskas, S. Paek, V. Jankauskas, M. K. Nazeeruddin, *Angew. Chem. Int. Ed*. **2016**, *55*, 7464.

[26] H. L. Chen, W. F. Fu, C. Y. Huang, Z. Q. Zhang, S. X. Li, F. Z. Ding, M. M. Shi, C. Z. Li, A. K. Y. Jen, H. Z. Chen, *Adv. Energy Mater*. **2017**, *7*, 1700012.

[27] R. A. Belisle, P. Jain, R. Prasanna, T. Leijtens, M. D. McGehee, *ACS Energy Lett*. **2016**, *1*, 556.

[28] K. Rakstys, S. Paek, P. Gao, P. Gratia, T. Marszalek, G. Grancini, K. T. Cho, K. Genevicius, V. Jankauskas, W. Pisula, M. K. Nazeeruddin, *J. Mater. Chem. A* **2017**, *5*, 7811.

[29] S. A. Ok, B. Jo, S. Somasundaram, H. J. Woo, D. W. Lee, Z. Li, B. G. Kim, J. H. Kim, Y. J. Song, T. K. Ahn, S. Park, H. J. Park, *Nat. Commun*. **2018**, *9*, 4537.

[30] a) Z. A. Li, Z. L. Zhu, C. C. Chueh, S. B. Jo, J. D. Luo, S. H. Jang, A. K. Y. Jen, *J. Am. Chem. Soc*. **2016**, *138*, 11833; b) P. Xu, P. Liu, Y. Li, B. Xu, L. Kloo, L. Sun, Y. Hua,

ACS Appl. Mater. Interfaces **2018**, *10*, 19697; c) H. Zhang, Y. Wu, W. Zhang, E. Li, C. Shen, H. Jiang, H. Tian, W.-H. Zhu, *Chem. Sci.* **2018**, *9*, 5919.

[31] Q. Q. Ge, J. Y. Shao, J. Ding, L. Y. Deng, W. K. Zhou, Y. X. Chen, J. Y. Ma, L. J. Wan, J. N. Yao, J. S. Hu, Y. W. Zhong, *Angew. Chem. Int. Ed.* **2018**, *57*, 10959.

[32] a) P. Agarwala, D. Kabra, *J. Mater. Chem. A* **2017**, *5*, 1348; b) H. D. Pham, Z. Wu, L. K. Ono, S. Manzhos, K. Feron, N. Motta, Y. Qi, P. Sonar, *Adv. Electron. Mater.* **2017**, *3*, 1700139; c) H. D. Pham, T. T. Do, J. Kim, C. Charbonneau, S. Manzhos, K. Feron, W. C. Tsoi, J. R. Durrant, S. M. Jain, P. Sonar, *Adv. Energy Mater.* **2018**, *8*, 1703007.

[33] a) I. Zimmermann, J. Urieta-Mora, P. Gratia, J. Arago, G. Grancini, A. Molina-Ontoria, E. Orti, N. Martin, M. K. Nazeeruddin, *Adv. Energy Mater.* **2016**, *16*, 1601674; b) H. D. Pham, H. Hu, K. Feron, S. Manzhos, H. Wang, Y. M. Lam, P. Sonar, *Solar RRL* **2017**, *1*, 1700105; c) H. D. Pham, H. Hu, F.-L. Wong, C.-S. Lee, W.-C. Chen, K. Feron, S. Manzhos, H. Wang, N. Motta, Y. M. Lam, P. Sonar, *J. Mater. Chem. C* **2018**, *6*, 9017.

[34] J. Cao, Y. M. Liu, X. J. Jing, J. Yin, J. Li, B. Xu, Y. Z. Tan, N. F. Zheng, *J. Am. Chem. Soc.* **2015**, *137*, 10914.

[35] Y. Lin, L. Shen, J. Dai, Y. Deng, Y. Wu, Y. Bai, X. Zheng, J. Wang, Y. Fang, H. Wei, W. Ma, X. C. Zeng, X. Zhan, J. Huang. *Adv. Mater.* **2017**, *29*, 1604545.

[36] a) M. Y. Zhang, S. X. Dai, S. Chandrabose, K. Chen, K. Liu, M. C. Qin, X. H. Lu, J. M. Hodgkiss, H. P. Zhou, X. W. Zhan, *J. Am. Chem. Soc.* **2019**, *140*, 14938; b) W. Chen, Y. Wang, G. Pang, C. W. Koh, A. B. Djurišić, Y. Wu, B. Tu, F. Liu, R. Chen, H. Y. Woo, X. Guo, Z. He, *Adv. Funct. Mater.* **2019**, *29*, 1808855.

[37] M. Stolterfoht, C. M. Wolff, J. A. Marquez, S. S. Zhang, C. J. Hages, D. Rothhardt, S. Albrecht, P. L. Burn, P. Meredith, T. Unold, D. Neher, *Nat. Energy* **2018**, *3*, 847.

[38] X. Guo, N. Zhou, S. J. Lou, J. Smith, D. B. Tice, J. W. Hennek, R. P. Ortiz, J. T. L. Navarrete, S. Li, J. Strzalka, L. X. Chen, R. P. H. Chang, A. Facchetti, T. J. Marks, *Nat. Photonics* **2013**, *7*, 825.

[39] D. He, L. Qian, L. Ding, *Polym. Chem.* **2016**, *7*, 2329.

[40] B. Xu, E. Sheibani, P. Liu, J. B. Zhang, H. N. Tian, N. Vlachopoulos, G. Boschloo, L. Kloo, A. Hagfeldt, L. C. Sun, *Adv. Mater.* **2014**, *26*, 6629.

[41] X. Q. Jiang, D. P. Wang, Z. Yu, W. Y. Ma, H. B. Li, X. C. Yang, F. Liu, A. Hagfeldt, L. C. Sun, *Adv. Energy Mater.* **2019**, *9*, 1803287.

[42] C. Bi, Q. Wang, Y. C. Shao, Y. B. Yuan, Z. G. Xiao, J. S. Huang, *Nat. Commun.* **2015**, *6*, 7747.

[43] K. Rakstys, A. Abate, M. I. Dar, P. Gao, V. Jankauskas, G. Jacopin, E. Kamarauskas, S. Kazim, S. Ahmad, M. Grätzel, M. K. Nazeeruddin, *J. Am. Chem. Soc*. **2015**, *137*, 16172.

[44] X. C. Wang, J. Zhang, S. W. Yu, W. Yu, P. Fu, X. Liu, D. D. Tu, X. Guo, C. Li, *Angew. Chem. Int. Ed*. **2018**, *57*, 12529.

[45] Y. Hua, B. Xu, P. Liu, H. Chen, H. N. Tian, M. Cheng, L. Kloo, L. C. Sun, *Chem. Sci*. **2016**, *7*, 2633.

[46] M. Saliba, T. Matsui, J. Y. Seo, K. Domanski, J. P. Correa-Baena, M. K. Nazeeruddin, S. M. Zakeeruddin, W. Tress, A. Abate, A. Hagfeldt, M. Grätzel, *Energy Environ. Sci*. **2016**, *9*, 1989.

[47] Y. H. Shao, Z. G. Xiao, C. Bi, Y. B. Yuan, J. S. Huang, *Nat. Commun*. **2014**, *5*, 5784.

[48] W. Tress, *Adv. Energy Mater*. **2017**, *7*, 1602358.

[49] R. Wang, M. Mujahid, Y. Duan, Z.-K. Wang, J. Xue, Y. Yang, *Adv. Funct. Mater*. **2019**, *29*, 1808843.

[50] B. Park, S. I. Seok, *Adv. Mater*. DOI: 10.1002/adma.201805337.

a

- *Adv. Energy Mater.*, 2016, *6*, 1502101 — *12.4%*
- *Adv. Energy Mater.*, 2017, *7*, 1700012 — *16.6%*
- *J. Mater. Chem. A*, 2017, *5*, 13220 — *17.54%*
- *Chem. Sci.*, 2018, *9*, 2698 — *17.01%*
- This work — *21.17%*
- *J. Am. Chem. Soc.*, 2016, *138*, 2528 — *18.6%* (R = C₆H₁₃)
- *Nano. Energy*, 2017, *41*, 10 — *15.7%* (R = C₈H₁₇)
- *Adv. Funct. Mater.*, 2017, *27*, 1702613 — *18.8%*
- *J. Am. Chem. Soc.*, 2018, *140*, 5018 — *17.2%*

2016 2017 2018 2019

b

hole-transporting units
passivation groups
appropriate π-π stacking
high dipole moment
MPA-BTI
MPA-BTTI

Figure 1. (a) Recent development of small molecule hole-transporting materials utilized in dopant-free inverted perovskite solar cells. (b) Schematic diagram of our molecular design principles and the corresponding chemical structures reported in this work.
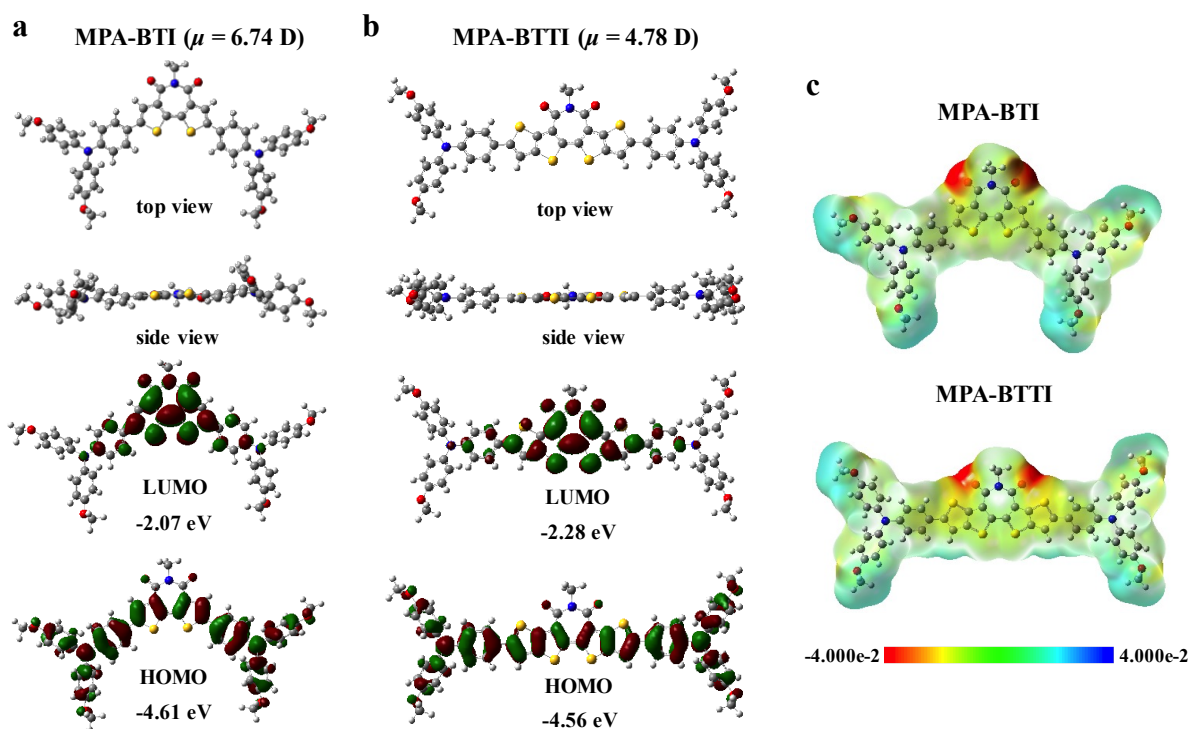
Figure 2. DFT calculation results of the HTMs MPA-BTI and MPA-BTTI. (a,b) Optimized ground state molecular configurations and corresponding HOMO and LUMO profiles for MPA-BTI and MPA-BTTI, respectively. (c) Electrostatic potential (ESP) surface for MPA-BTI and MPA-BTTI. For simplicity, long alkyl chains are replaced by methyl group.
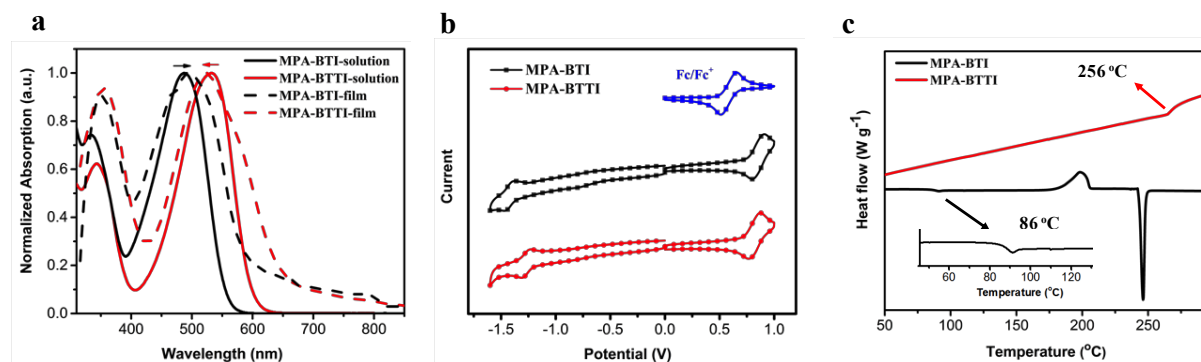
Figure 3. Optical, electrochemical and thermal properties of HTMs. (a) Ultraviolet-visible absorption spectra of MPA-BTI and MPA-BTTI both in solution (10^{-5} mol L^{-1}) and solid state. (b) Cyclic voltammograms of MPA-BTI and MPA-BTTI measured in CH_2Cl_2 solution using the ferrocene/ferrocenium redox couple (Fc/Fc$^+$) as the reference with a scanning rate of 50 mV s^{-1}. (c) DSC curves of MPA-BTI and MPA-BTTI during the second heating scan which was measured at a heat ramp of 10 $^{\circ}$C min^{-1}.
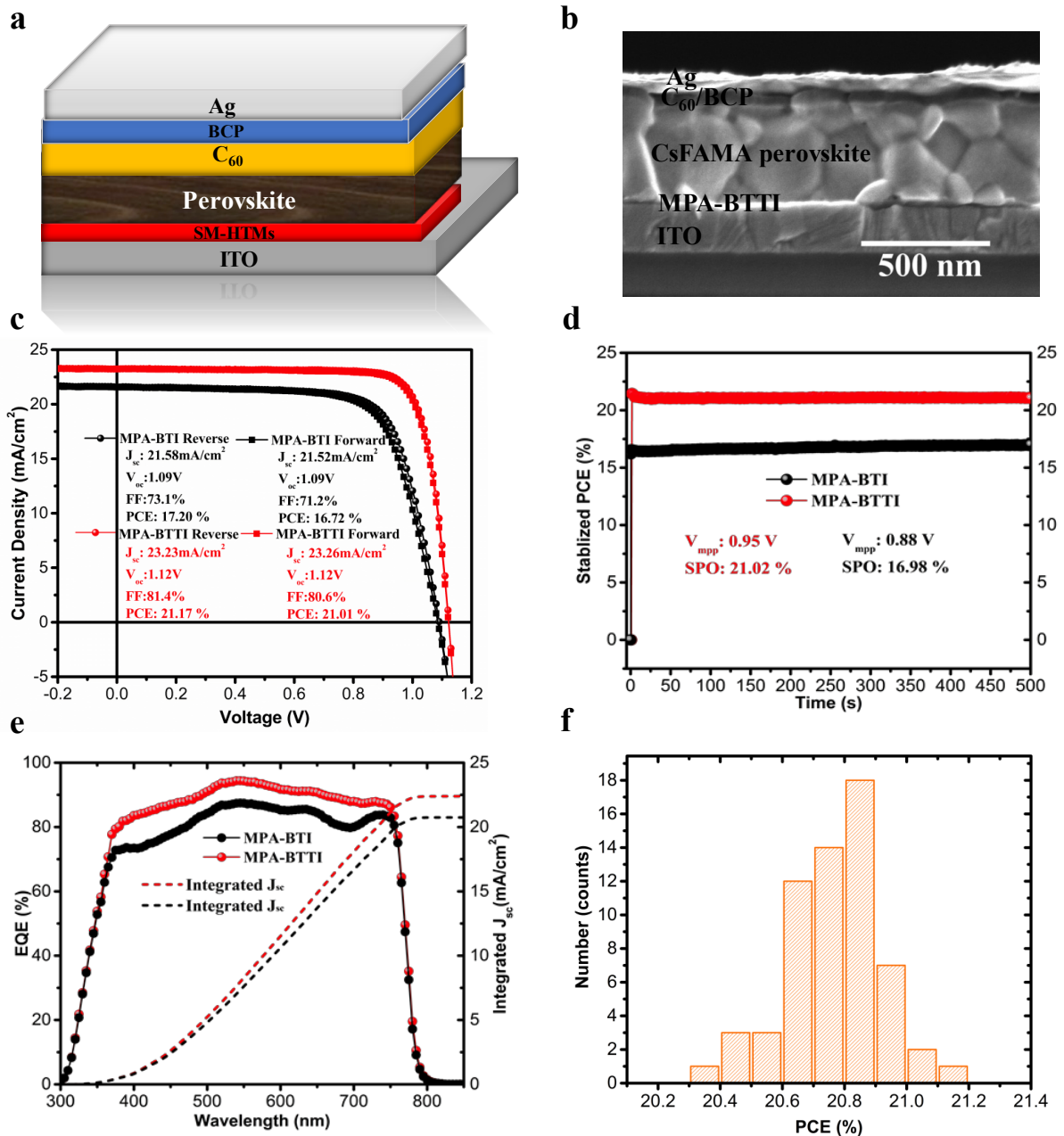
Figure 4. Device structure, cross-section SEM and device performance. (a) Schematic diagram of the device structure with *p-i-n* (inverted) configuration. (b) Cross-section SEM images of the MPA-BTTI based PVSCs. (c) The *J-V* curves of the best performing MPA-BTI and MPA-BTTI based solar cells. (d) Stabilized PCE measurement of the best device for MPA-BTI and MPA-BTTI. (e) External quantum efficiency (EQE, solid circles) with the integrated short-circuit current density (dash lines) for the MPA-BTI and MPA-BTTI based cells. (f) PCE histograms of 60 devices from different batches utilizing MPA-BTTI as the HTM.
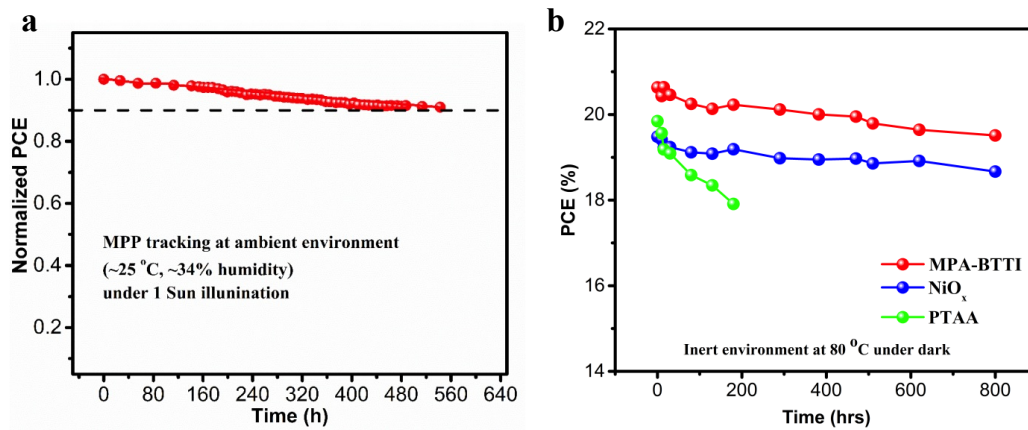
Figure 5. Device stability. (a) The evolution of normalized power conversion efficiency obtained from MPA-BTTI based device with encapsulation at ambient environment (~25 °C, 34% humidity) under maximum power point (MPP) tracking and continuous light irradiation (AM 1.5 G, 100 mW cm^{-2}, white LED). (b) Long-term thermal stability of MPA-BTTI based device stressed at 80 °C in inert environment in the dark.

Table 1. Optical, electrochemical, thermal, and charge transport properties of MPA-BTI and MPA-BTTI.

	$\lambda_{abs,sol}$ (nm) [a]	$\lambda_{abs,film}$ (nm)	E_g^{opt} (eV) [b]	HOMO (eV) [c]	LUMO (eV) [d]	E_g^{CV} (eV) [e]	T_d (^{o}C)	T_g (^{o}C)	μ (D) [f]	λ_h (eV) [g]	μ_h (cm^2 V^{-1} s^{-1})	Conductivity (S cm^{-1})
MPA-BTI	335, 487	351, 496	2.12	-5.28	-3.15	2.13	432	86	6.74	0.18	3.99×10^{-5}	6.90×10^{-6}
MPA-BTTI	343, 532	357, 522	1.92	-5.24	-3.32	1.92	431	256	4.78	0.15	2.02×10^{-4}	1.35×10^{-5}

[a] Measured in THF solution with a concentration of 10^{-5} mol/L. [b] Estimated from the absorption edge in neat film using the equation: $E_g^{opt} = 1243 / \lambda_{onset}$ (eV). [c] $E_{HOMO} = -5.1-(E_{ox} -E_{1/2}$ (Fc/Fc$^+$)) (eV). [d] $E_{LUMO} = -5.1-(E_{red} -E_{1/2}$ (Fc/Fc$^+$)) (eV). [e] Electrochemical bandgap from CV measurements. [f] Dipole moment calculated by DFT. [g] Hole reorganization energies calculated by DFT.

Table 2. Device performance parameters of the best-performing PVSCs with MPA-BTI and MPA-BTTI as the dopant-free HTMs.

HTMs	Devices	V_{oc} (V)	J_{sc} (mA/cm^2)	*FF* (%)	PCE (%)
MPA-BTI	forward scan	1.09	21.52	0.712	16.72
	reverse scan	1.09	21.58	0.731	17.20
MPA-BTTI	forward scan	1.12	23.26	0.806	21.01
	reverse scan	1.12	23.23	0.814	21.17

Two novel donor-acceptor type hole-transporting materials were developed and characterized. Due to the good energy level alignment, appropriate hole-transporting ability, and most importantly, the excellent film morphology, the MPA-BTTI based dopant-free inverted perovskite solar cell exhibits a remarkable PCE of 21.17% with negligible hysteresis and long-time operational stability.

Keyword: Small molecule, Hole-transporting material, Dopant-free, Inverted perovskite solar cells

Yang Wang, Wei Chen, Lei Wang, Bao Tu, Tian Chen, Bin Liu, Kun Yang, Chang Woo Koh, Xianhe Zhang, Huiliang Sun, Guocong Chen, Xiyuan Feng, Han Young Woo, Aleksandra B. Djurišić,* Zhubing He* and Xugang Guo*

Dopant-Free Small Molecule Hole-transporting Material for Inverted Perovskite Solar Cells with Efficiency Exceeding 21%

ToC figure
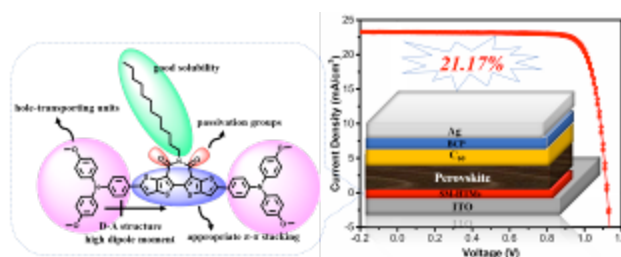
WILEY-VCH

((Supporting Information can be included here using this template))

Supporting Information

Dopant-Free Small Molecule Hole-transporting Material for Inverted Perovskite Solar Cells with Efficiency Exceeding 21%

Yang Wang, Wei Chen, Lei Wang, Bao Tu, Tian Chen, Bin Liu, Kun Yang, Chang Woo Koh, Xianhe Zhang, Huiliang Sun, Guocong Chen, Xiyuan Feng, Han Young Woo, Aleksandra B. Djurišić,* Zhubing He* and Xugang Guo*

Dr. Y. Wang, W. Chen, Dr. L. Wang, B. Tu, T. Chen, B. Liu, Dr. K. Yang, X. Zhang, Dr. H. Sun, G. Chen, X. Feng, Prof. Z. He, Prof. X. Guo

Department of Materials Science and Engineering, Southern University of Science and Technology (SUSTech), No. 1088, Xueyuan Road, Shenzhen, Guangdong 518055, China.

E-mail: hezb@sustech.edu.cn; guoxg@sustech.edu.cn

W. Chen, Prof. A. B. Djurišić

Department of Physics, The University of Hong Kong, Pokfulam, Hong Kong SAR.

E-mail: dalek@hku.hk

C. W. Koh, Prof. H. Y. Woo

Department of Chemistry, Korea University, Seoul 02841, South Korea.

Dr. Y. Wang

Key Laboratory of Functional Polymer Materials and State Key Laboratory of Medicinal Chemical Biology, The Co-Innovation Center of Chemistry and Chemical Engineering of Tianjin, Institute of Polymer Chemistry, College of Chemistry, Nankai University, Tianjin 300071, China.

ORCID

Yang Wang: 0000-0002-3669-0192

Han Young Woo: 0000-0001-5650-7482

Aleksandra B. Djurišić: 0000-0002-5183-1467

Xugang Guo: 0000-0001-6193-637X

Zhubing He: 0000-0002-2775-0894

1. Characterization and measurements

The ^{1}H NMR and ^{13}C NMR spectra were recorded on the Bruker Ascend 400 MHz spectrometer. High-resolution mass spectra were obtained with ThermoScientificTM Q-Exactive. Elemental analyses (EAs) of compounds were performed at Shenzhen University (Shenzhen, Guangdong, China). UV-Vis optical absorption spectra of solutions (in THF) and thin films were recorded on a Shimadzu UV-3600 UV-VIS-NIR spectrophotometer. Cyclic voltammetry measurements were carried out under argon atmosphere using the CHI760E voltammetric workstation with a N_2-saturated solution of 0.1 M tetra-n-butyl ammonium hexafluoro phosphate (Bu$_4$NPF$_6$) in CH$_2$Cl$_2$ as the supporting electrolyte. A platinum disk working electrode, a platinum wire counter electrode, and a silver wire reference electrode were employed, and the ferrocene/ferrocenium redox couple (Fc/Fc$^+$) was used as the reference for all measurements with a scanning rate of 50 mV s^{-1}. Thermogravimetric (TGA) measurements were carried out on a METTLER TOLEDO (TGA 1 STARe System) apparatus at a heat ramp of 10 ^{o}C min^{-1} under N_2. DSC curves were recorded on a differential scanning calorimetry in nitrogen (Mettler, STARe, heating ramp: 10 ^{o}C min^{-1}). Atomic Force Microscopy (AFM) measurements were conducted using a Dimension Icon Scanning Probe Microscope (Asylum Research, MFP-3D-Stand Alone) in the tapping mode. 2D GIWAXS measurements were carried out at the PLS-II 9A U-SAXS beam line of Pohang Accelerator Laboratory, Korea.

2. Computational details

The geometry optimization and quantum chemical calculation including dipole moments and hole reorganization energy of MPA-BTI and MPA-BTTI were performed by the DFT/B3LYP method with 6-31(d) basis sets. TD-DFT was used with 6-31(d) to get the electronic transition energies and simulate the corresponding absorption spectra using the PCM solvent model in THF. All the calculations were carried out using Gaussian 09 program package.

3. Device fabrication

Perovskite solar cells (PVSCs) with a *p-i-n* structure were fabricated with a configuration of ITO/HTMs/perovskite/C$_{60}$/BCP/Ag. ITO glass was cleaned by sequentially washing with detergent, deionized water, acetone, and isopropanol (IPA). The substrates were dried with N_2 and cleaned by UV ozone for 15 min. MPA-BTI and MPA-BTTI HTMs with a concentration of 3.5 mg/mL in toluene were spin coated on the clean ITO substrates and annealed at 80 ^{o}C and 110 ^{o}C for 10 min, respectively. Other HTMs including NiO$_x$ NPs, PEDOT:PSS and PTAA were prepared according to the reported procedures[S1-S3]. The CsFAMA mixed

perovskite layers were fabricated according to our previously reported one-step antisolvent method[S1]. After the perovskite growth, the substrates were transferred into high vacuum thermal evaporator where the C_{60} (30 nm), BCP (8 nm) and Ag (120 nm) were subsequently evaporated. The active area was controlled using a shadow mask.

4. Device characterization

J-V measurements were carried out using a Keithley 2400 source meter in ambient environment at ~25 ºC and ~45% RH. The devices were measured both in reverse scan (1.2 V→-0.2 V, step 0.01 V) and forward scan (-0.2 V→1.2 V, step 0.01 V) with 10 ms delay time. Illumination was provided an Oriel Sol3A solar simulator with AM1.5G spectrum and light intensity of 100 mW/cm^2 was calibrated by a standard KG-5 Si diode. The active area (14.25 mm^2) of our device was calibrated with a shadow mask during the measurements. EQE measurements for devices were conducted with an Enli-Tech (Taiwan) EQE measurement system. Top-view morphology was analyzed by TESCAN MIRA3, and cross-section SEM was characterized by Helios Nanolab 600i FIB. The X-ray diffraction patterns were obtained using a BRUKER ECO D8 series. Time resolved PL spectra were measured using a Spectrofluorometer (FS5, Edinburgh instruments) and 405 nm pulsed laser was used as excitation source for the measurement.

5. Device stability test

For the maximum power point (MPP) tracking test, the encapsulated solar cell was fixed at the V_{mpp} and the current density variation under ambient environment (~25 ºC, 34% RH) was recorded. 10 min interval was selected to record the value of current density. For thermal tests, the devices were stored in inert environment with O_2 < 0.1 ppm and H_2O < 0.1 ppm at room temperature and/or 80 ºC. The devices were kept in the dark except for the I-V measurement, and the I-V curves were recorded in certain time intervals. For stability test under illumination, encapsulated devices were mounted on a sample holder under inert (N_2 gas) environment and the cells were illuminated constantly with simulated solar illumination at 1 sun intensity.

6. Synthesis of MPA-BTI and MPA-BTTI

All reagents and chemicals are commercially purchased and are used without further purification unless otherwise stated. Solvents were purified by standard methods and dried if necessary. Synthetic routes could be found in Figure S1. Dithieno[3,2-c:2',3'-e]oxepine-4,6-dione (compound **1**)[S4] and 4-methoxy-N-(4-methoxyphenyl)-N-(4-(4,4,5,5-tetramethyl-1,3,2-dioxaborolan-2-yl)phenyl)aniline (compound **4**)[S5] were synthesized based on the previously described procedures. Thieno [2',3':4,5]thieno[3,2-c]thieno[2',3':4,5]thieno [2,3-e]oxepine-4,6-dione (compound **5**) was prepared according to the methods reported in literature[S6].

Synthesis of 5-octyl-4H-dithieno[3,2-c:2',3'-e]azepine-4,6(5H)-dione (compound **2**). To a 50 mL flask was charged with compound **1** (100 mg, 0.42 mmol), *n*-octylamine (82 mg, 0.63 mmol), 4-dimethylaminopyridine (77 mg, 0.63 mmol), and 1,4-dioxane (6 mL), and the combined mixture was heated to reflux for 12 h. Then acetic anhydride (10 mL) was injected in one portion, and the reaction was heated to reflux for another 3h. After cooling to room temperature, all the solvent was removed and the crude product was purified by column chromatography (silica gel, petroleum ether:CH_2Cl_2 = 2:1 as the eluent), affording the compound **2** (100 mg, 68% yield) as a yellow solid.

^{1}H NMR (400MHz, $CDCl_3$): δ 7.76 (*d*, *J* = 5.4 Hz, 2H), 7.25 (*d*, *J* = 5.4 Hz, 2H), 4.23-4.19 (m, 2H), 1.75-1.62 (m, 2H), 1.43-1.29 (m, 10H), 0.89 (*t*, *J* = 6.8 Hz, 3H).

Synthesis of 2,8-dibromo-5-octyl-4H-dithieno[3,2-c:2',3'-e]azepine-4,6(5H)-dione (compound **3**). Compound **2** (200 mg, 0.57 mmol) was dissolved in $CHCl_3$ (7 mL), followed by the addition of $FeCl_3$ (2 mg, 0.01 mmol) and bromine (0.1 mL, 367 mg, 2.3 mmol). After stirring for 3 h at room temperature, water was added to quench the reaction, and the mixture was extracted with $CHCl_3$ three times. The combined organic layer was dried over anhydrous Na_2SO_4. After the removal of solvent, the pure product **3** (260 mg, 90% yield) was obtained by column chromatography (silica gel, petroleum ether:CH_2Cl_2 = 4:1).

^{1}H NMR (400MHz, $CDCl_3$): δ 7.71 (s, 2H), 4.18-4.14 (m, 2H), 1.69-1.65 (m, 2H), 1.38-1.27 (m, 10H), 0.90 (*t*, *J* = 6.8 Hz, 3H).

Synthesis of 2,8-bis(4-(bis(4-methoxyphenyl)amino)phenyl)-5-octyl-4H-dithieno 3,2-c:2',3'-e]azepine-4,6(5H)-dione (**MPA-BTI**). To a 100 mL dried flask was charged with compound **3** (150 mg, 0.3 mmol), compound **4** (367 mg, 0.78 mmol), $Pd(PPh_3)_4$ (35 mg, 0.03 mmol), K_2CO_3 (126 mg, 0.9 mmol), H_2O (2 mL), and THF (14 mL), and heated to reflux for 24 h under a nitrogen atmosphere. After cooling to room temperature, the reaction mixture was extracted with CH_2Cl_2 three times. The combined organic layer was dried over anhydrous Na_2SO_4. After the solvent was evaporated, the residue was purified by column chromatography (silica gel, petroleum ether:CH_2Cl_2 = 2:1 as the eluent) to obtain a red powder in 56% yield (160 mg).

^{1}H NMR (400MHz, $CDCl_3$): δ 7.82 (s, 2H), 7.42 (*d*, *J* = 8.2 Hz, 4H), 7.12 (*d*, *J* = 8.4 Hz, 8H), 6.93 (*d*, *J* = 8.3 Hz, 4H), 6.89 (*d*, *J* = 8.6 Hz, 8H), 4.25-4.22 (m ,2H), 3.84 (s, 12H), 1.77-1.70 (m, 2H), 1.45-1.30 (m, 10H), 0.90 (*t*, *J* = 6.7 Hz, 1H).

^{13}C NMR (400MHz, $CDCl_3$): δ 161.68, 156.41, 149.37, 142.66, 140.07, 135.44, 133.27, 127.15, 126.55, 126.37, 123.82, 119.54, 114.86, 55.51, 46.30, 31.87, 29.39, 29.33, 27.78, 27.35, 22.69, 14.15.

HRMS: $C_{58}H_{55}N_3O_6S_2$ calcd: 953.3532, found: 953.3517. Elemental Analysis: C, 73.01; H, 5.81; N, 4.40; S, 6.72, Found: C, 73.21; H, 5.70; N, 4.30; S, 6.78.

Synthesis of 5-dodecyl-4H-thieno[2',3':4,5]thieno[3,2-c]thieno[2',3':4,5]thieno [2,3-e]azepine-4,6(5H)-dione (compound **6**) was performed using a similar procedure as described for compound **2**. Yield: 82%.

^{1}H NMR (400MHz, CDCl$_3$): δ 7.63 (*d*, *J* = 5.3 Hz, 2H), 7.30 (*d*, *J* = 5.4 Hz, 2H), 4.43-4.36 (m, 2H), 1.85-1.78 (m, 2H), 1.51-1.28 (m, 18H), 0.90 (*t*, *J* = 6.8 Hz, 3H).

Synthesis of 2,8-dibromo-5-dodecyl-4H-thieno[2',3':4,5]thieno[3,2-c]thieno [2',3':4,5]thieno[2,3-e]azepine-4,6(5H)-dione (compound **7**). Compound **6** (200 mg, 0.38 mmol) was dissolved in CHCl$_3$ (7 mL), followed by the addition of *N*-bromosuccinimide (208 mg, 1.16 mmol) in DMF (2 mL) solution. The mixture was stirred at room temperature for 12 h and then poured into water. The mixture was extracted with CHCl$_3$ three times, and the combined organic layer was dried over anhydrous Na$_2$SO$_4$. After the solvent was evaporated, the residue was purified by column chromatography (silica gel, petroleum ether:CH$_2$Cl$_2$ = 3:1 as the eluent) to afford an orange solid as the target product in 80% yield (204 mg).

^{1}H NMR (400MHz, CDCl$_3$): δ 7.22 (s, 2H), 4.32-4.29 (m, 2H), 1.80-1.72 (m, 2H), 1.46-1.28 (m, 18H), 0.89 (*t*, *J* = 6.8 Hz, 3H).

Synthesis of 2,8-bis(4-(bis(4-methoxyphenyl)amino)phenyl)-5-dodecyl-4H-thieno [2',3':4,5]thieno[3,2-c]thieno[2',3':4,5]thieno[2,3-e]azepine-4,6(5H)-dione (**MPA- BTTI**) was carried out according to the similar procedure as described for **MPA-BTI**. Yield: 48%.

^{1}H NMR (400MHz, CDCl$_3$): δ 7.43 (*d*, *J* = 8.7 Hz, 4H), 7.24 (s, 2H), 7.07 (*d*, *J* = 8.9 Hz, 8H), 6.89 (*d*, *J* = 8.7 Hz, 4H), 6.86 (*d*, *J* = 9.0 Hz, 8H), 4.39-4.35 (m, 2H), 3.83 (s, 12H), 1.86-1.82 (m, 2H), 1.50-1.28 (m, 18H), 0.90 (*t*, *J* = 6.8 Hz, 3H).

^{13}C NMR (400MHz, CDCl$_3$): δ 160.12, 156.23, 150.87, 148.86, 141.03, 140.19, 138.51, 135.05, 127.07, 126.35, 125.57, 124.54, 119.64, 114.79, 111.98, 55.48, 46.42, 31.96, 29.80, 29.72, 29.68, 29.59, 29.40, 27.62, 27.47, 22.72, 14.16.

HRMS: $C_{66}H_{63}N_3O_6S_4$ calcd: 1121.3600, found: 1122.3678 [M+H]. Elemental Analysis: C, 70.62; H, 5.66; N, 3.74; S, 11.42, Found: C, 70.51; H, 5.71; N, 3.70; S, 11.40.

Table S1. Summary of recent developments of dopant-free small molecule hole-transporting materials utilized in inverted perovskite solar cells.

HTMs	V_{oc} (V)	J_{sc} (mA/cm^2)	FF	PCE (%)	Ref.
DFTAB	1.07	17.5	0.69	12.4	[S7]
CzPAF-TPA	1.05	20.0	0.74	15.7	[S8]
TPP-SMeTAD	1.07	20.15	0.77	16.6	[S9]
BTF4	1.03	21.5	0.76	17.01	[S10]
3-F-br-4C	1.06	20.2	0.80	17.2	[S11]
TPAC3M	1.00	22.79	0.78	17.54	[S12]
Trux-OMeTAD	1.02	23.2	0.79	18.6	[S13]
TAPC	1.04	22.32	0.81	18.8	[S14]
MPA-BTTI	**1.12**	**23.23**	**0.813**	**21.17**	**This work**
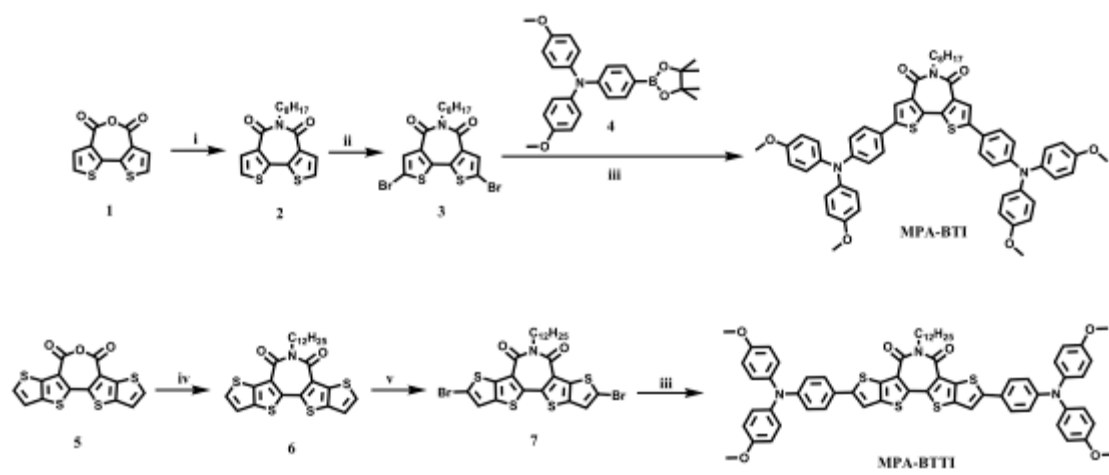
Figure S1. Chemical structures and detailed synthetic routes to **MPA-BTI** and **MPA-BTTI**. Reagents and conditions: i) *n*-octylamine, 4-dimethylaminopyridine, 1,4-dioxane, acetic anhydride, reflux; ii) Br_2, $FeCl_3$, $CHCl_3$, room temperature; iii) Compound **4**, $Pd(PPh_3)_4$, K_2CO_3, THF, H_2O, reflux; iv) 1-dodecylamine, 4-dimethylaminopyridine, 1,4-dioxane, acetic anhydride, reflux; v) *N*-bromosuccinimide, DMF, $CHCl_3$, room temperature.

a)

b)
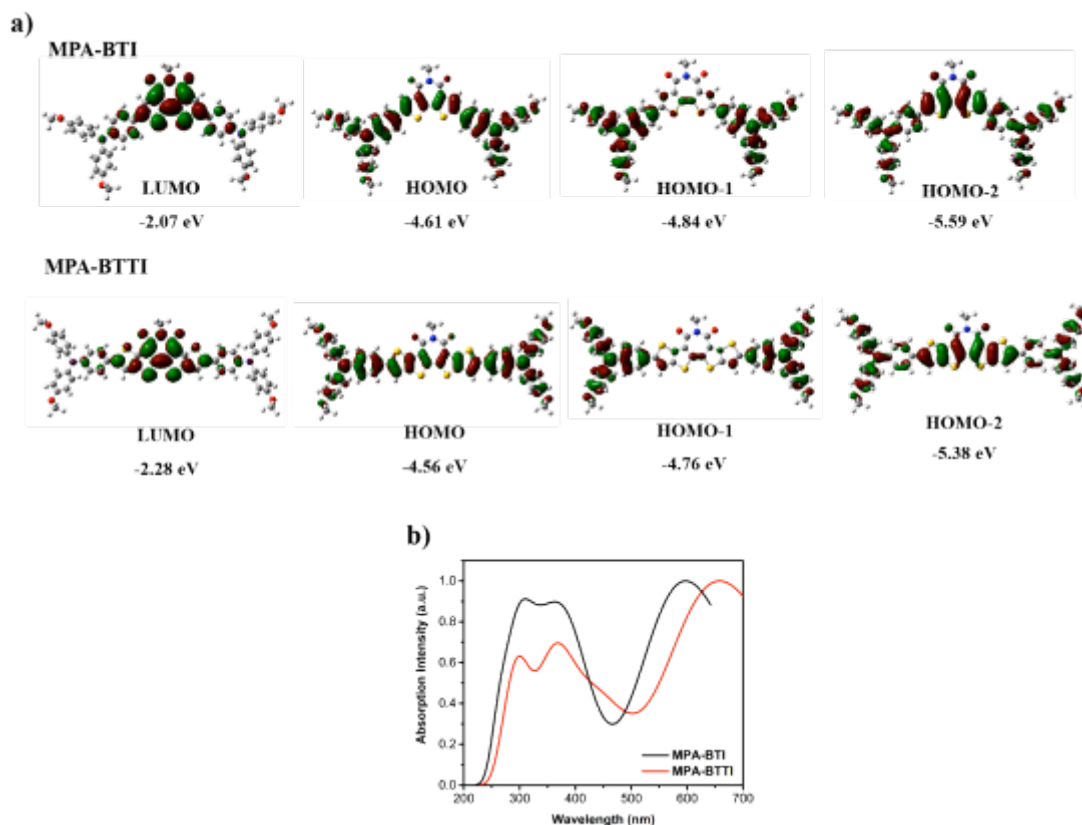
Figure S2. (a) Contours and energy levels of LUMO and the first three occupied molecular orbitals for MAP-BTI and MPABTTI, (b) Simulated absorption spectra calculated by B3LYP/6-31g(d) method with the PCM solvent model in THF. For simplicity, long alkyl chains are replaced by methyl group.

Table S2. The key electronic absorption spectra properties of MAP-BTI and MPABTTI.

HTMs	Excited state	λ(nm)	Oscillator strength	Configuration
MPA-BTI	S_1	601.45	1.0753	HOMO → LUMO (98%)
	S_3	402.51	0.4094	HOMO-2 → LUMO (95%)
MPA-BTTI	S_1	658.77	1.5662	HOMO → LUMO (98%)
	S_3	452.47	0.5660	HOMO-2 → LUMO (97%)

Table S3. The corresponding hole reorganization energy (λ_h) obtained from DFT method.[a]

HTMs	IP(v) (eV)	HEP (eV)	λ_h (eV)
MPA-BTI	5.45	5.27	0.18
MPA-BTTI	5.33	5.18	0.15

[a] The internal hole reorganization energy (λ_h) can be expressed as λ_h = IP(v) – HEP, where IP(v) stands for vertical ionization potential and HEP stands for hole extraction potential.[S15]
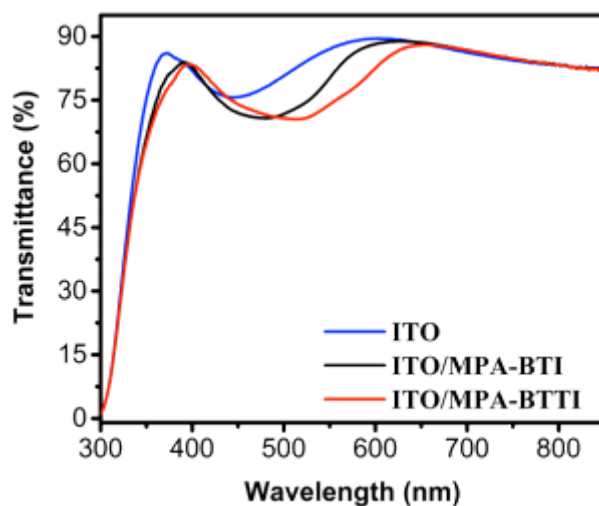
Figure S3. UV-Vis transmittance of MPA-BTI and MPA-BTTI films (~10 nm) on ITO substrates. Transmittance spectrum of bare ITO substrate is also shown.
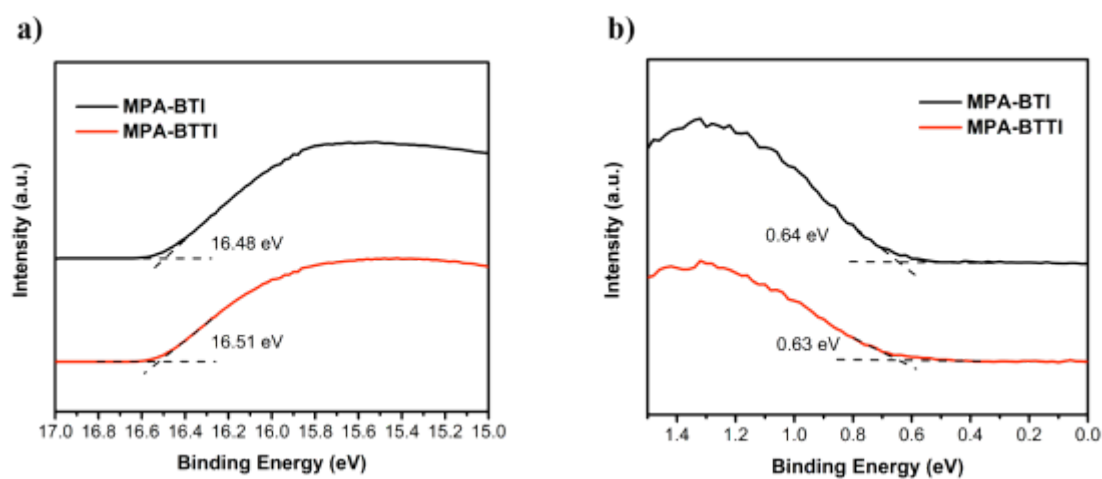
Figure S4. UPS spectra in the cutoff (a) and the onset (b) energy regions of MPA-BTI and MPA-BTTI films.
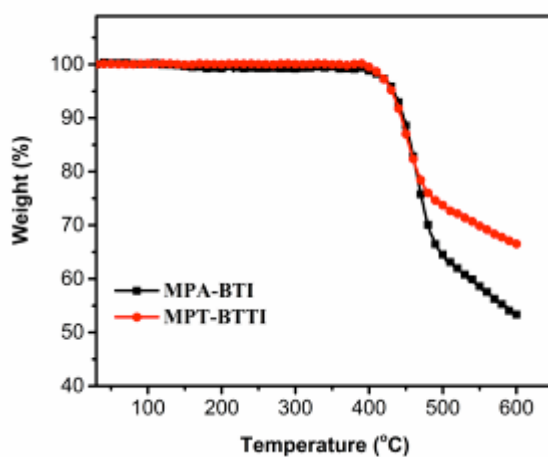
Figure S5. Thermal gravimetric curves of MPA-BTI and MPA-BTTI.
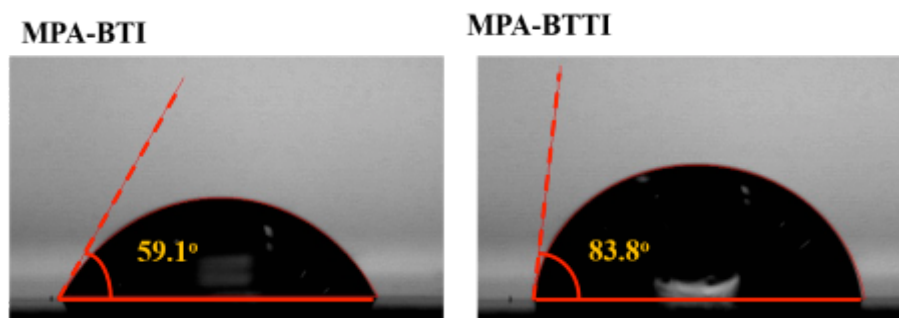
Figure S6. Water contact angles on MPA-BTI and MPA-BTTI films.
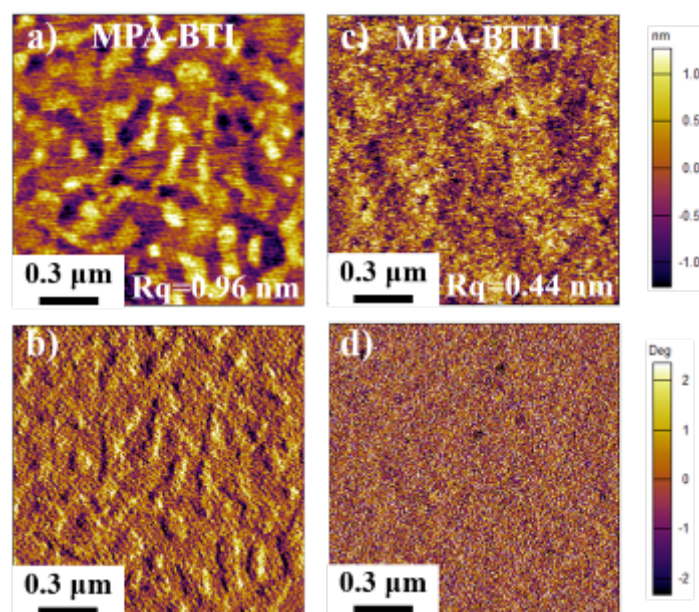
Figure S7. AFM height (a, c) and phase images (b, d) of MPA-BTI and MPA-BTTI films which were spin-coated on ITO substrates and annealed at 80 ºC and 110 ºC, respectively.
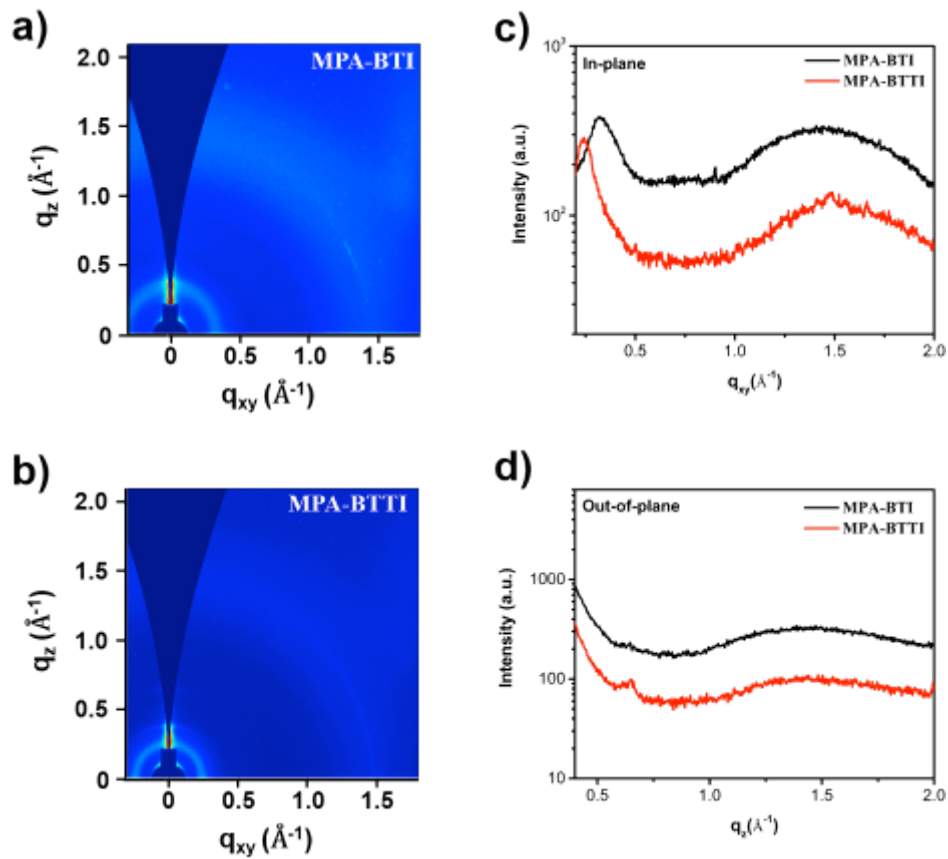
Figure S8. 2D-GIWAXS patterns of (a) MPA-BTI and (b) MPA-BTTI films after thermal annealing, and (c, d) the corresponding line-cut profiles along the in-plane and out-of-plane directions.
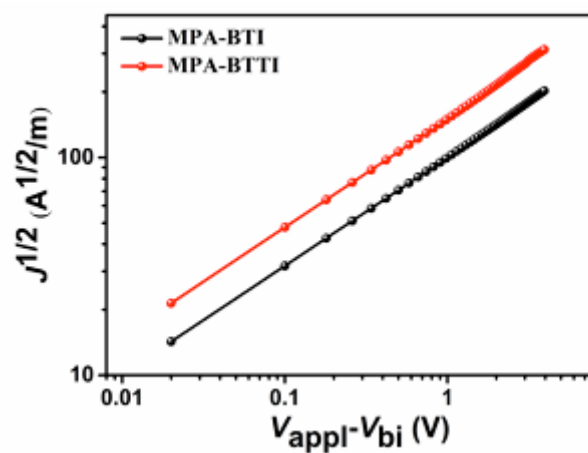
Figure S9. The corresponding $J^{1/2}$-V curves for the hole-only devices based on the pure films of MPA-BTI and MPA-BTTI.
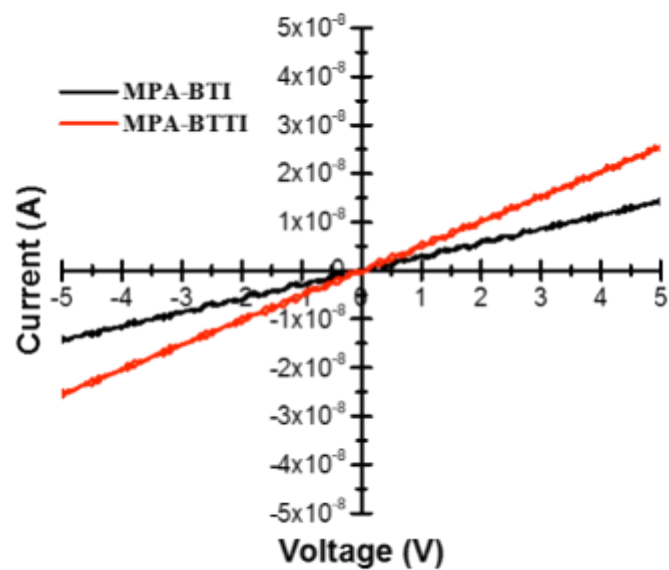
Figure S10. Conductivity measured for the neat MPA-BTI and MPA-BTTI films.
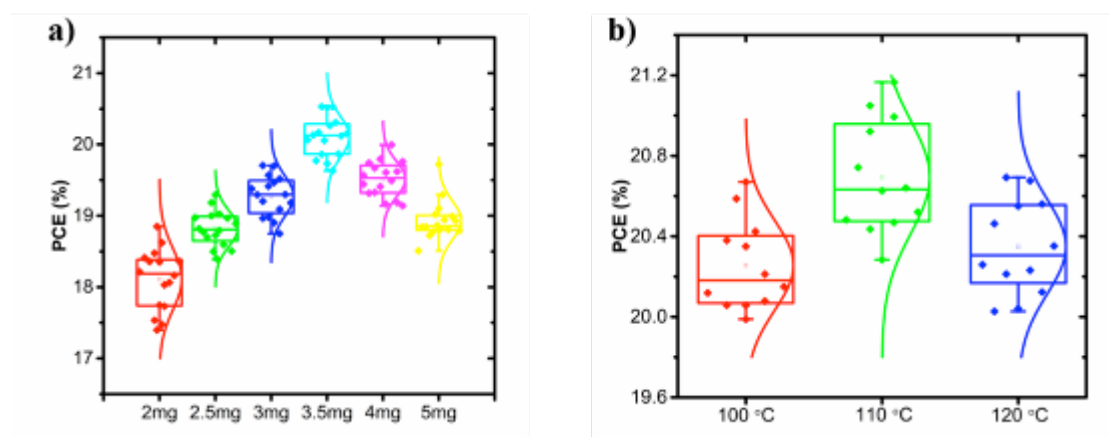
Figure S11. Optimization of the MPA-BTTI based solar cells. a) PCE dependence on solution concentration, b) PCE dependence on annealing temperature.
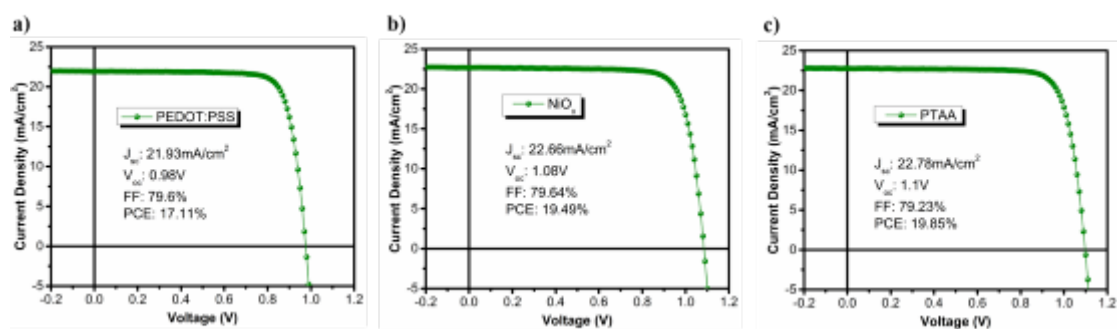
Figure S12. Current-voltage curves and device performance parameters (inset) of the optimal perovskite solar cells based on several widely-used HTMs such as a) PEDOT:PSS, b) NiO_x, and c) PTAA.

Table S4. Device performance parameters of the CsFAMA based perovskite solar cells with different HTMs.

HTMs	V_{oc} (V)	J_{sc} (mA/cm^2)	FF (%)	PCE (%)
PEDOT:PSS	0.98	21.93	0.796	17.11
NiO_x	1.08	22.66	0.796	19.49
PTAA	1.10	22.78	0.792	19.85
MPA-BTTI	1.12	23.23	0.813	21.17

a)

b)
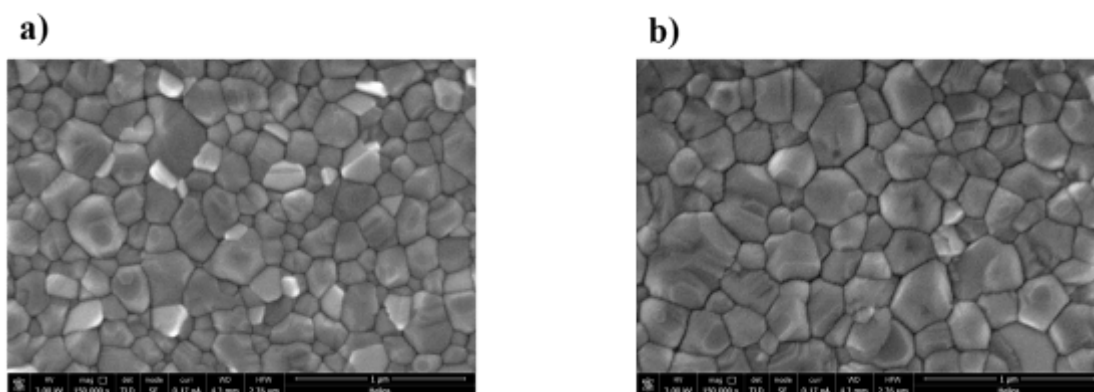
Figure S13. Top view scanning electron microscopy (SEM) images of perovskite films prepared on a) MPA-BTI and b) MPA-BTTI.
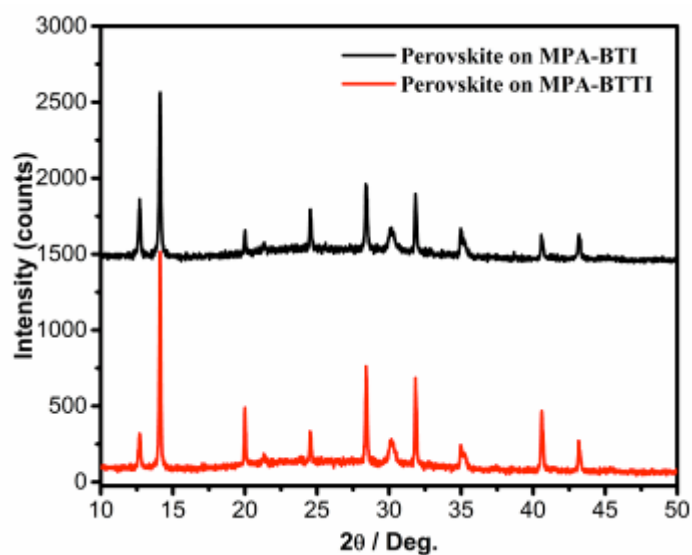
Figure S14. X-ray diffraction patterns of the CsFAMA perovskite films grown on MPA-BTI and MPA-BTTI.
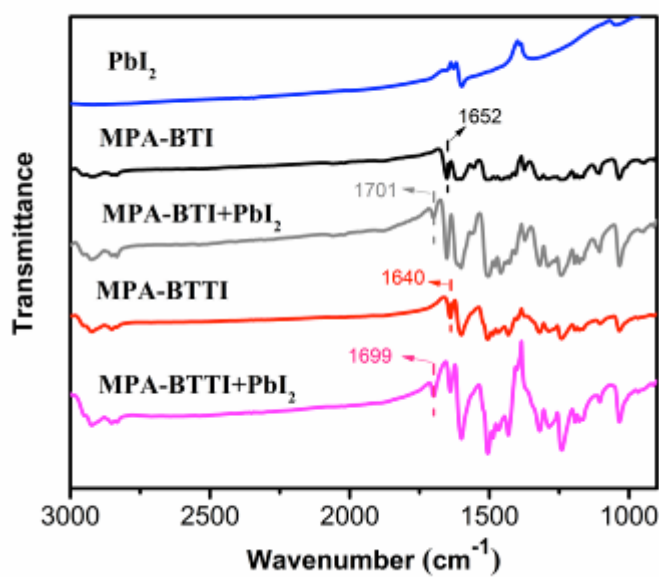
Figure S15. FTIR spectra of MPA-BTI and MPA-BTTI with PbI$_2$ films (pure PbI$_2$, MPA-BTI and MPA-BTTI films as the control).
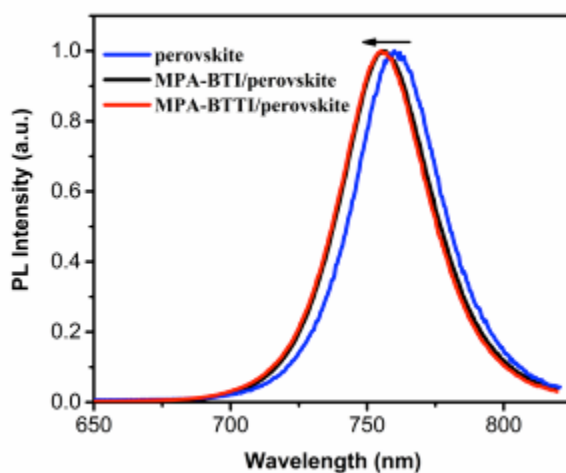
Figure S16. Photoluminescence spectra of perovskite, MPA-BTI/perovskite and MPA-BTTI/perovskite films with normalized intensity at room temperature.
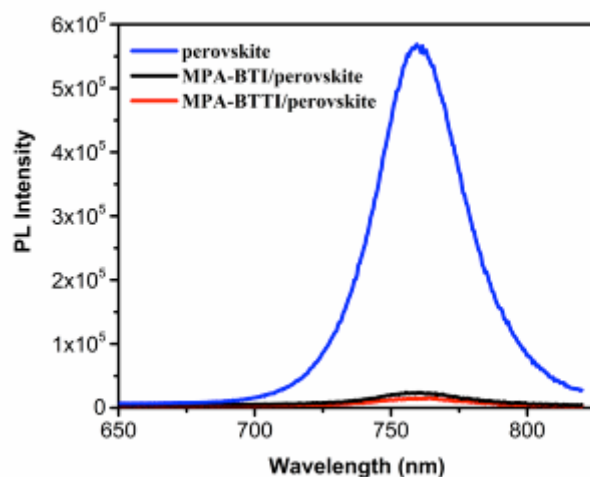
Figure S17. Steady-state photoluminescence spectra of perovskite, MPA-BTI/perovskite and MPA-BTTI/perovskite films.
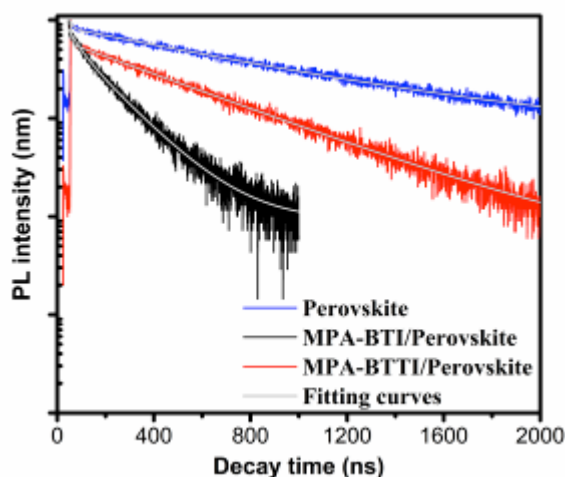
Figure S18. Time-resolved photoluminescence measurements of the perovskite films on different substrates.

Table S5. Fitted parameters of photoluminescence decay curves of perovskite grown on ITO substrate, MPA-BTI and MPA-BTTI, respectively.

Sample	A_1 (%)	τ_1 (ns)	A_2 (%)	τ_2 (ns)	τ_{avg} (ns) [a]
ITO/perovskite	2.4	12.4	97.6	822.8	822.5
ITO/MPA-BTI/perovskite	35.6	46.5	64.4	171.8	155.5
ITO/MPA-BTTI/perovskite	65.5	3.3	34.5	484.2	478.0

[a] τ_{avg} refers to average lifetime which is calculated as following: $\tau_{avg} = (A_1\tau_1^2 + A_2\tau_2^2)/(A_1\tau_1 + A_2\tau_2)$.
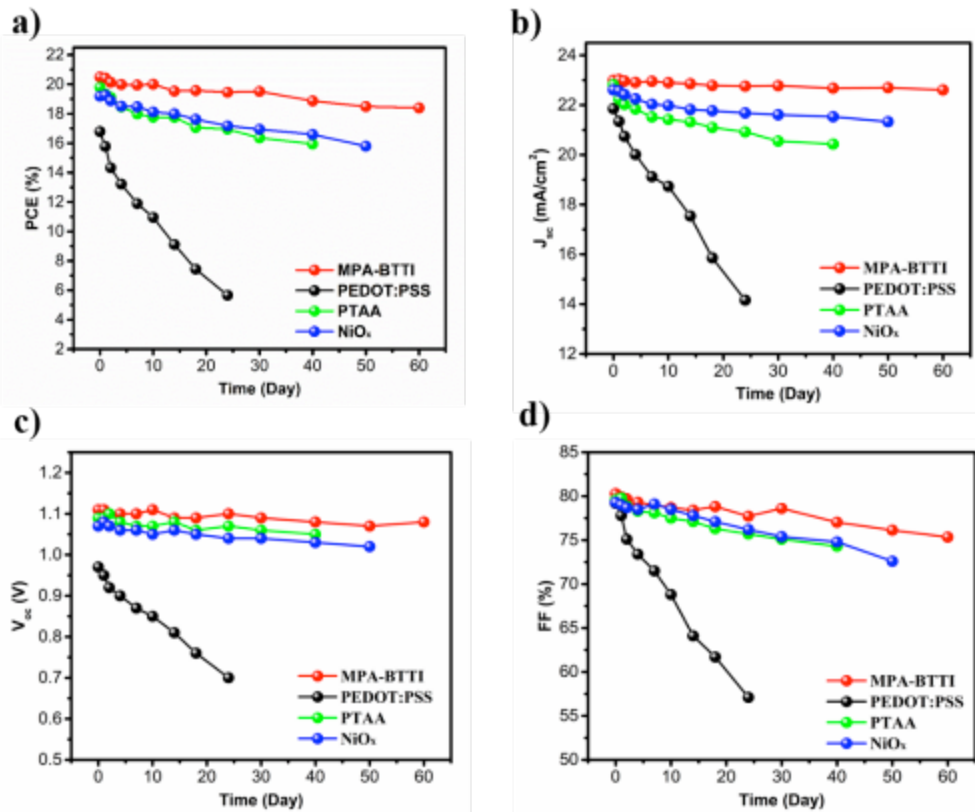
Figure S19. Comparative evolution of a) PCE, b) J_{sc}, c) V_{oc}, and d) FF of perovskite solar cells with different HTMs, *i.e.* MPA-BTTI, PEDOT:PSS, PTAA and NiO$_x$, stored in a dry box (20% RH) at room temperature in the dark. Initial efficiencies are 20.49%, 16.78%, 19.79%, and 19.18% for MPA-BTTI, PEDOT:PSS, PTAA and NiO$_x$ based devices, respectively, which were measured from *J-V* curves.
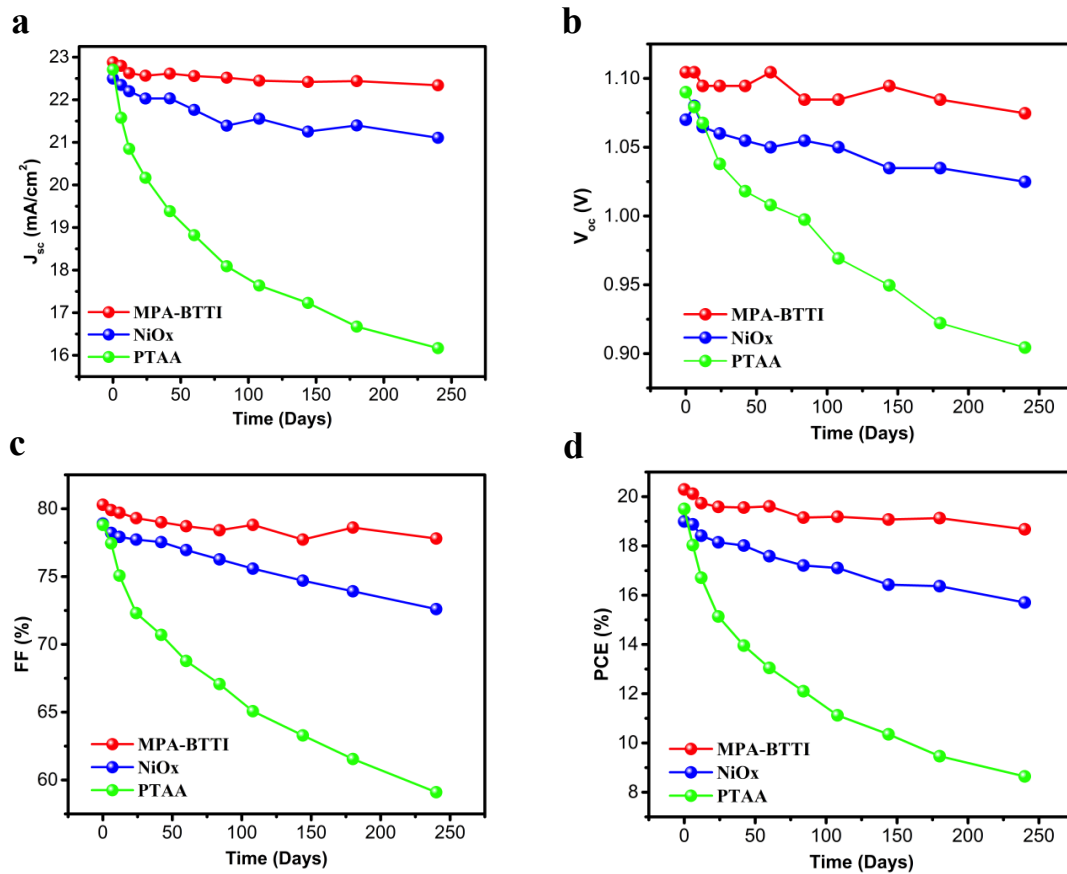
Figure S20. Comparative evolution of a) J_{sc}, b) V_{oc}, c) FF, and d) PCE for the MPA-BTTI, NiO$_x$ and PTAA based perovskite solar cell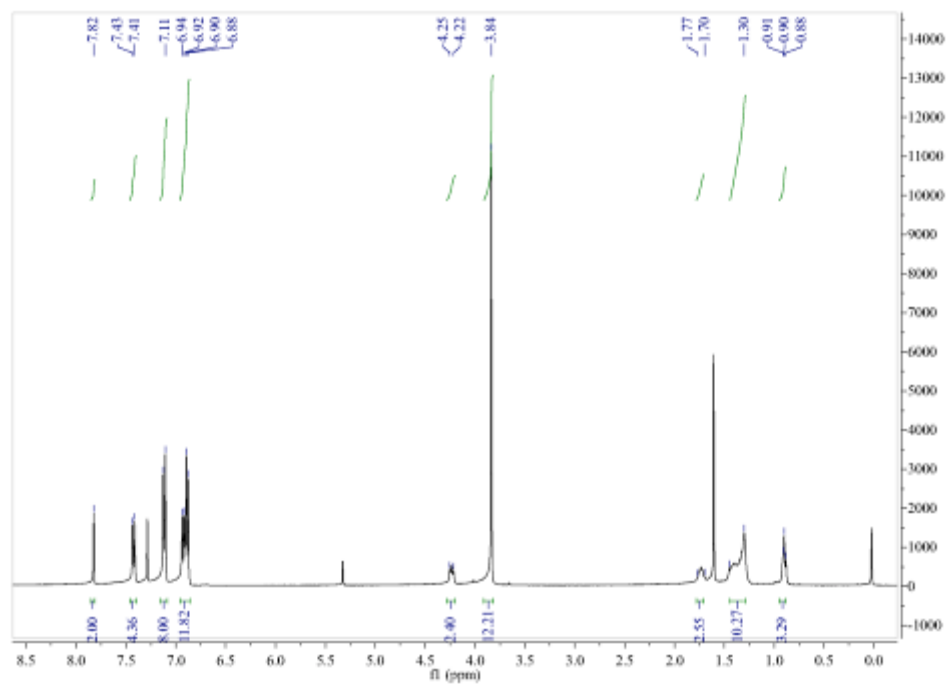s stressed under light illumination in an inert environment. Data were obtained from the I-V scans at certain time intervals.
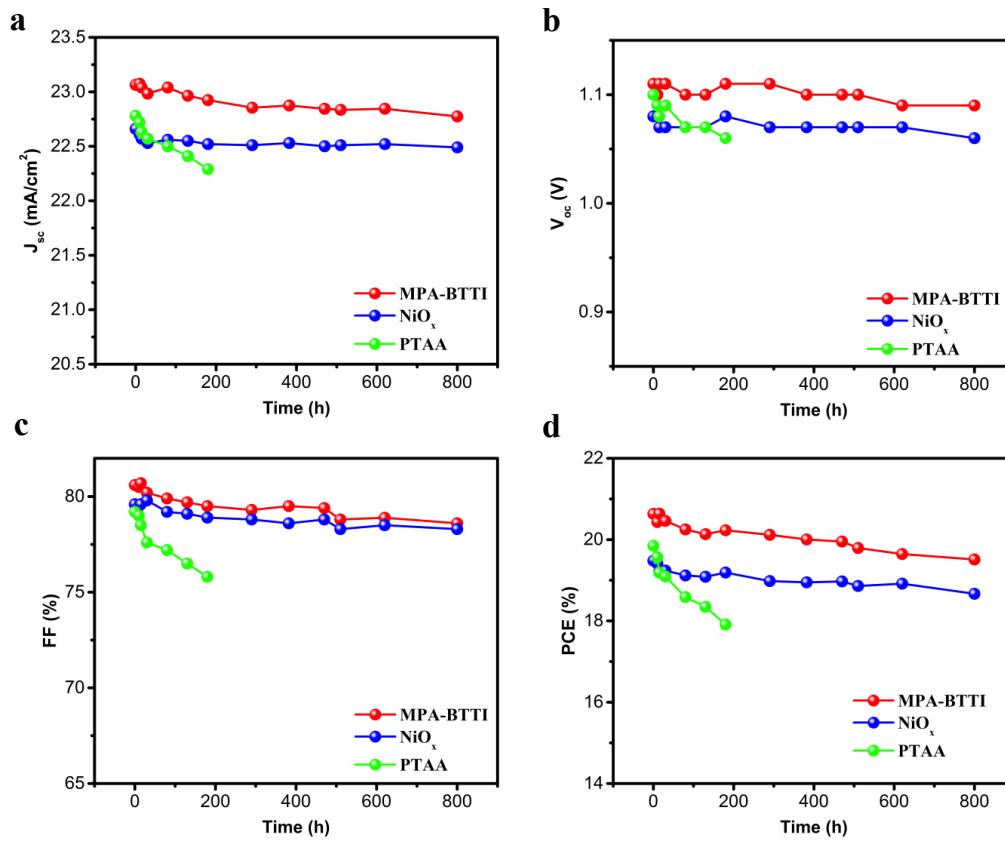
Figure S21. Comparative evolution of a) J_{sc}, b) V_{oc}, c) FF, and d) PCE for the MPA-BTTI, NiO$_x$ and PTAA based perovskite solar cells stressed at 80 °C in the dark and in an inert environment.
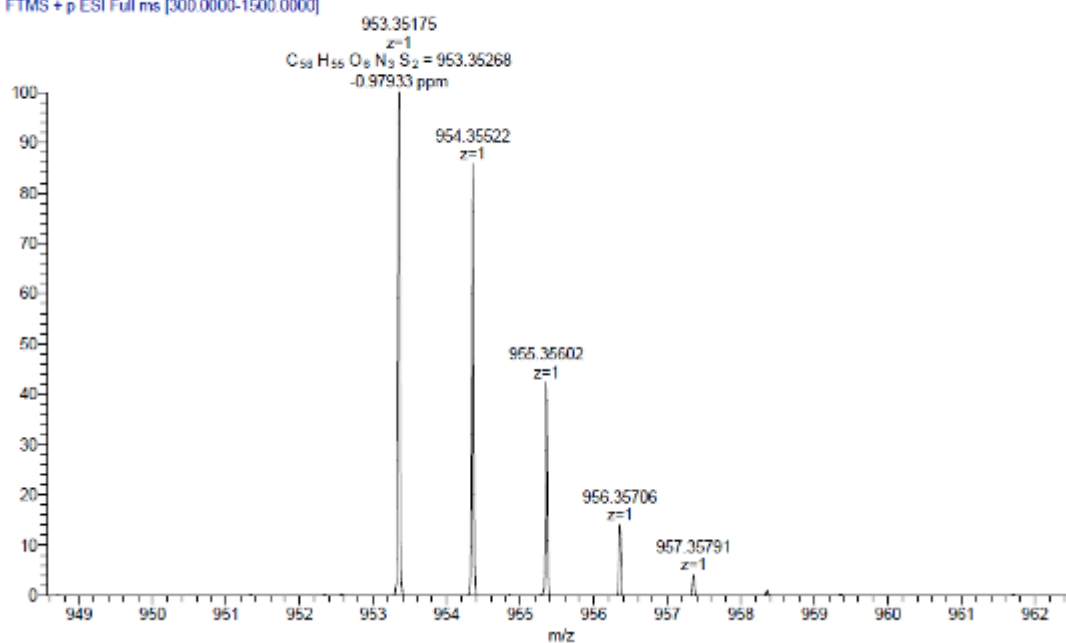
Figure S22. ^{1}H NMR spectrum of **MPA-BTI**.
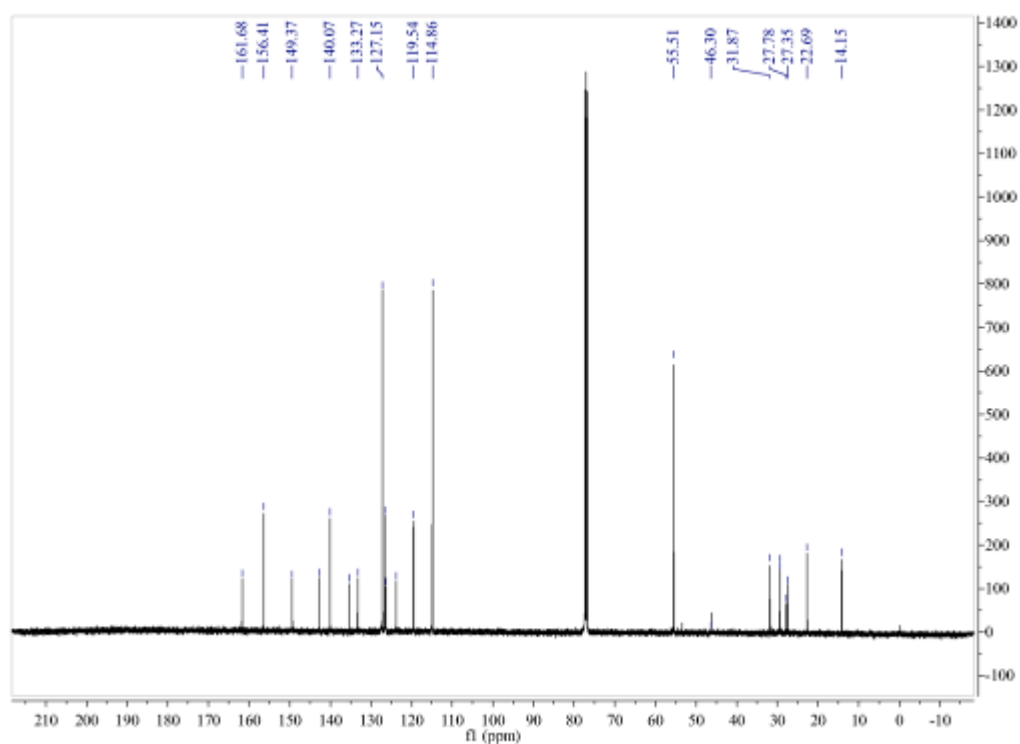
Figure S23. ^{13}C NMR spectrum of **MPA-BTI**.

[C58H55N3O6S2]⁺

WY-R293 181112155544 #9 RT: 0.12 AV: 1 NL: 4.09E7
T: FTMS + p ESI Full ms [300.0000-1500.0000]
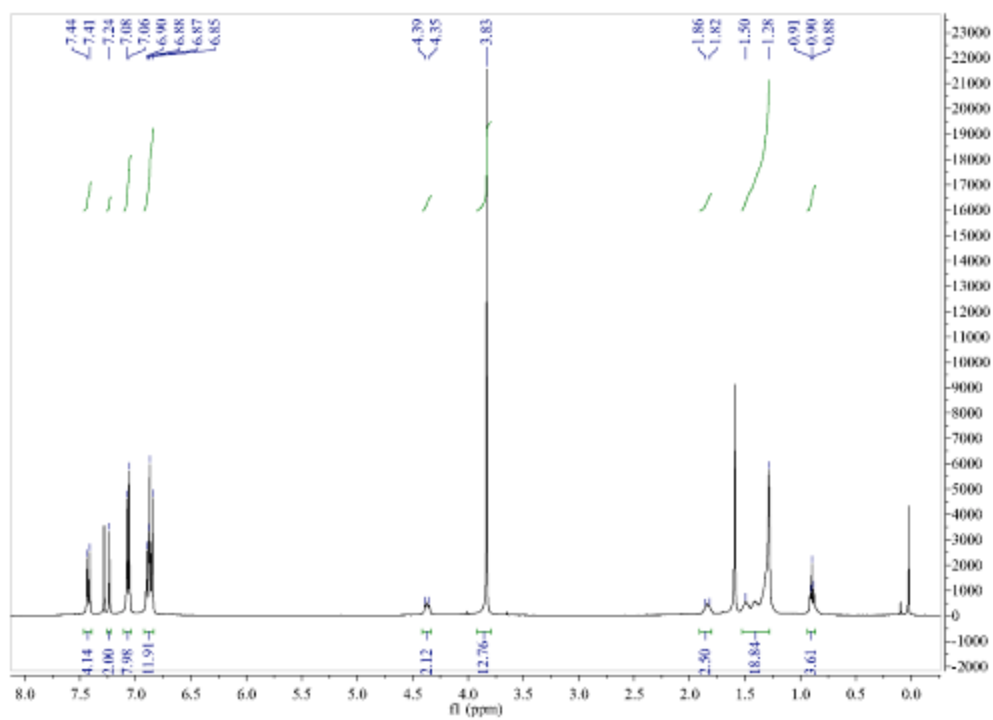

Figure S24. HRMS spectrum of **MPA-BTI**.
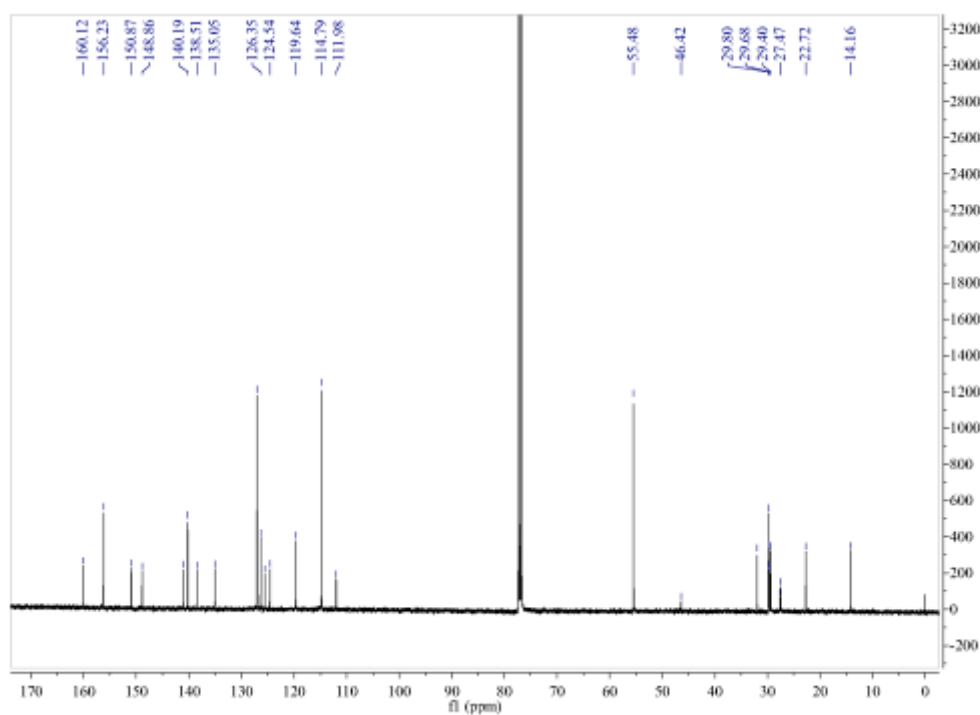
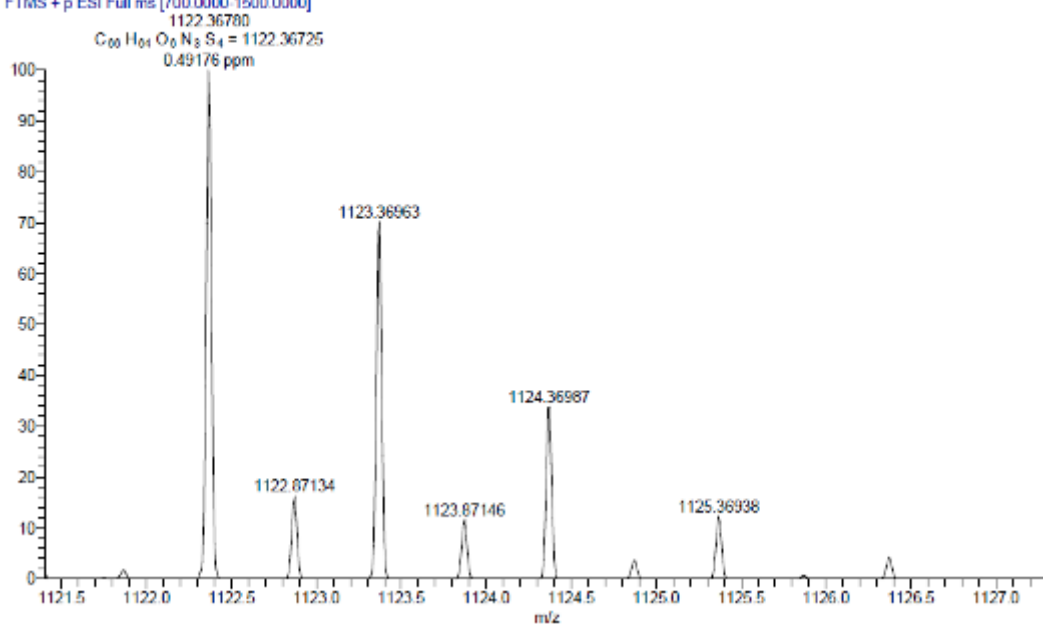**Figure S25**. ^{1}H NMR spectrum of **MPA-BTTI**.

Figure S26. ^{13}C NMR spectrum of **MPA-BTTI**.

Figure S27. HRMS spectrum of **MPA-BTTI**.

References

[S1] W. Chen, Y. Zhou, L. Wang, Y. Wu, B. Tu, B. Yu, F. Liu, H.-W. Tam, G. Wang, A. B. Djurišic´, L. Huang, Z. He, *Adv. Mater.* **2018**, *30*, 1800515.

[S2] W. Chen, L. Xu, X. Feng, J. Jie, Z. He, *Adv. Mater.* **2017**, *29*, 1603923.

[S3] W. Chen, Y. Zhu, Y. Yu, L. Xu, G. Zhang, Z. He, *Chem. Mater.* **2016**, *28*, 4879-4883.

[S4] X. Guo, et. al. *Nat. Photonics* **2013**, *7*, 825-833.

[S5] L. Chen, B. Zhang, Y. Cheng, Z. Xie, L. Wang, X. Jing, F. Wang, *Adv. Funct. Mater.* **2010**, *20*, 3143-3153.

[S6] D. He, L. Qian, L. Ding, *Polym. Chem.* **2016**, *7*, 2329-2332.

[S7] A. El Labban, H. Chen, M. Kirkus, J. Barbe, S. Del Gobbo, M. Neophytou, I. McCulloch, J. Eid, *Adv. Energy Mater.* **2016**, *6*, 1502101.

[S8] S. S. Reddya, S. Shina, U. K. Aryala, R. Nishikubob, A. Saekib, M. Songc, S.-H. Jina, *Nano. Energy* **2017**, *41*, 10-17.

[S9] H. Chen, W. Fu, C. Huang, Z. Zhang, S. Li, F. Ding, M. Shi, C.-Z. Li, A. K.-Y. Jen, H. Chen, *Adv. Energy Mater.* **2017**, *7*, 1700012.

[S10] X. Sun, Q. Xue, Z. Zhu, Q. Xiao, K. Jiang, H.-L. Yip, H. Yan, Z. Li, *Chem. Sci.* **2018**, *9*, 2698-2704.

[S11] R. Shang, Z. M. Zhou, H. Nishioka, H. Halim, S. Furukawa, I. Takei, N. Ninomiya, E. Nakamura, *J. Am. Chem. Soc.* **2018**, *140*, 5018-5022.

[S12] S. J. Park, S. Jeon, I. K. Lee, J. Zhang, H. Jeong, J. Y. Park, J. Bang, T. K. Ahn, H. W. Shin, B. G. Kim, H. J. Park, *J. Mater. Chem. A* **2017**, *5*, 13220-13227.

[S13] C. Y. Huang, W. F. Fu, C. Z. Li, Z. Q. Zhang, W. M. Qiu, M. M. Shi, P. Heremans, A. K. Y. Jen, H. Z. Chen, *J. Am. Chem. Soc.* **2016**, *138*, 2528-2531.

[S14] L. Y. Yang, F. L. Cai, Y. Yan, J. H. Li, D. Liu, A. J. Pearson, T. Wang, *Adv. Funct. Mater.* **2017**, *27*, 1702613.

[S15] Y. Wang, Z. Zhu, C.-C. Chueh, A. K.-Y. Jen, Y. Chi, *Adv. Energy Mater.* **2017**, *7*, 1700823.